Computer Modeling in Engineering & Sciences

Tech Science Press

https://doi.org/10.32604/cmes.2026.088992

ARTICLE

Interpretable Machine Learning Framework for Safety Factor Prediction of Pile-Reinforced Slopes Based on Physical Tests and Finite Element Simulations

Jingqiu Yang[1], Wei Li[2], Huan Zheng[2], Jinlong Pan[3], Jun Jiang[2] and Li Guo[3,*]

[1]Yunnan Power Grid Co., Ltd., Kunming Branch, Kunming, China
[2]Yunnan Power Grid Co., Ltd., Yuxi Power Supply Bureau, Yuxi, China
[3]School of Civil Engineering, Southeast University, Nanjing, China

*Corresponding Author: Li Guo. Email: lguo@seu.edu.cn

Received: 13 July 2026; Accepted: 11 September 2026; Published: 21 October 2026

ABSTRACT: Accurate and efficient prediction of the safety factor of pile-reinforced slopes is essential for stability assessment and preliminary reinforcement design. This study develops an experimental–numerical–data-driven framework for rapid and interpretable prediction. Physical model tests were conducted to investigate pile–soil interaction and soil arching under different pile-spacing conditions. A three-dimensional finite element model incorporating cohesion anisotropy was evaluated against the experimental observations and then used to generate a Sobol-sampled database of 1024 cases. Six variables describing soil properties and pile layout were considered, and twelve machine-learning models were systematically compared. MLP achieved the highest test-set accuracy (R^2 = 0.928), whereas KAN showed competitive performance (R^2 = 0.913) and statistically comparable sample-wise errors. KAN was retained as the representative model for database-size sensitivity, additional-case assessment, and SHAP interpretation, while MLP served as the accuracy-oriented benchmark. For KAN, cohesion and friction angle contributed 30.7% and 29.4% of the normalized mean absolute SHAP value, respectively, while pile diameter ranked third at 18.5%. An interactive prediction platform was also developed to integrate model inference, visualization, and SHAP-based explanation. The results provide an efficient tool for preliminary screening and comparison of pile-reinforcement alternatives within the defined domain.

KEYWORDS: Anti-slide pile; pile-reinforced slope; safety factor prediction; interpretable machine learning; SHAP

1 Introduction

Slope instability is one of the most common geotechnical hazards and may cause severe damage to infrastructure, transportation systems, and surrounding environments. Anti-slide piles have been widely used as an effective reinforcement measure for landslide control and slope stabilization. They transfer thrust from the sliding mass to the stable soil layer through pile–soil interaction. Compared with conventional retaining structures, pile reinforcement is particularly suitable for slopes where deep-seated deformation or localized sliding needs to be controlled. Therefore, accurately evaluating the stability of pile-reinforced slopes is essential for reinforcement design and risk assessment [1].

The mechanical behavior of pile-reinforced slopes is strongly governed by pile–soil interaction and the soil arching effect between adjacent piles [2]. Under the action of landslide thrust, the soil between piles redistributes the load and transfers part of the sliding force to the piles through arch-shaped stress paths. This mechanism is affected by pile spacing, pile diameter, pile position, and soil strength parameters. Previous

Copyright © 2026 The Authors. Published by Tech Science Press. This work is licensed under a Creative Commons Attribution 4.0 International License, which permits unrestricted use, distribution, and reproduction in any medium, provided the original work is properly cited.

studies have shown that pile spacing plays a critical role in the development of soil arching, and excessive pile spacing may weaken the cooperative constraint between adjacent piles [3,4]. However, the spatial evolution of soil arching and its influence on the overall safety factor of pile-reinforced slopes remain complex. They are jointly controlled by soil properties, pile layout, and nonlinear deformation.

Numerical methods, especially the finite element method, have become powerful tools for slope stability analysis. They capture stress redistribution, deformation, and progressive failure without requiring a predefined slip surface. In finite element-based slope stability analysis, the strength reduction method determines the safety factor by gradually reducing the shear-strength parameters until failure occurs [5–7]. For pile-reinforced slopes, three-dimensional modeling is usually required to capture pile–soil interaction and inter-pile soil arching. The arching effect depends on pile spacing, pile configuration, loading conditions, and soil properties [8]. In addition, natural sedimentary soils may exhibit inherent strength anisotropy caused by deposition-induced particle orientation, and ignoring this anisotropy may lead to inaccurate or even overestimated safety factors [9]. Nevertheless, repeated three-dimensional FEM strength reduction analyses remain computationally expensive, especially when a large number of parameter combinations must be evaluated for design optimization, uncertainty analysis, or database construction. Recent studies have therefore introduced machine-learning surrogate models to reduce the computational burden of repeated slope stability simulations [10].

Machine-learning models can learn nonlinear mappings between geotechnical parameters and safety factors from numerical or experimental databases, thereby enabling rapid prediction once the model has been trained [11–13]. Similar data-driven approaches have also been applied to other complex civil engineering problems, such as concrete corrosion assessment, demonstrating their broad capability in nonlinear response prediction [14–17]. Various models, such as decision trees, ensemble learning methods, support vector machines, neural networks, and gradient boosting algorithms, have been used for slope stability prediction [18–20]. These studies demonstrate the potential of machine learning in reducing computational cost and improving prediction efficiency [21–23]. Recent studies have further extended machine-learning-assisted slope stability analysis from deterministic safety factor (FS) prediction toward multi-source learning, probabilistic reliability assessment, and more advanced surrogate modelling. Tun et al. [24] compared several machine-learning algorithms using 1500 strength-reduction-based slope cases and reported strong FS prediction performance of MLP, SVM, and KNN. Chen et al. [25] proposed a multi-stage learning strategy that integrated historical slope data, numerical simulations, and physical experiments to jointly predict stability status, FS, and stability probability. For slopes with spatially variable soils, Huang et al. [26] developed an attention-enhanced convolutional surrogate model for efficient reliability analysis and interpretable assessment of spatial variability. More recently, Li et al. [27] introduced a graph-neural-network surrogate for slope reliability analysis, enabling efficient prediction of safety factors and potential slip surfaces under spatially variable soil conditions. These developments demonstrate a shift from conventional deterministic prediction toward multi-source, probabilistic, and interpretable machine-learning frameworks. However, most existing studies focus on ordinary soil slopes, while fewer studies consider pile-reinforced slopes involving three-dimensional pile–soil interaction, soil arching, and pile layout parameters.

Another challenge is the interpretability of machine-learning models [28]. Although complex models may achieve high prediction accuracy, their black-box nature limits their acceptance in geotechnical engineering, where physically meaningful interpretation is required for design decisions. SHAP provides a unified framework for explaining model predictions by assigning contribution values to input variables and has been increasingly used to interpret nonlinear machine-learning models [29,30]. In addition, Kolmogorov–Arnold networks have recently attracted attention as an alternative neural-network architecture [31]. These networks place learnable activation functions on edges instead of fixed activation

functions on nodes. This structure provides strong nonlinear approximation ability and potential interpretability, making KAN a promising approach for geotechnical regression problems involving complex parameter interactions.

Despite these advances, three gaps remain. First, most data-driven slope-stability studies address unreinforced slopes and do not explicitly represent three-dimensional pile–soil interaction or soil arching. Second, finite element surrogates are commonly evaluated mainly by predictive accuracy, with limited assessment of whether the learned relationships are mechanically interpretable. Third, the connection among physical observations, numerical database construction, model comparison, and deployable prediction remains fragmented. To address these gaps, this study develops an experimental–numerical–data-driven framework for interpretable *FS* prediction of pile-reinforced slopes. Its specific contributions are: (1) physical model observations of spacing-dependent soil arching and pile response; (2) a three-dimensional FEM model that incorporates cohesion anisotropy and is checked against multiple experimental response patterns; (3) a Sobol-sampled FEM database and comparison of twelve machine-learning models using accuracy and train–test stability; and (4) SHAP-based global and local explanations integrated into an interactive prediction system.

2 Physical Model Test of Pile-Reinforced Slopes

2.1 Experimental Setup

To investigate pile–soil interaction and soil arching effect in pile-reinforced slopes, a series of physical model tests were conducted in a rigid model box measuring 1600 mm × 1200 mm × 1000 mm. The model slope was constructed using sand, with a slope angle of 37°, a slope height of 600 mm, and a basal soil layer thickness of 397 mm. These dimensions were selected to provide sufficient space for the development of slope deformation and pile–soil interaction during loading.

The model piles were fabricated using Q235 hollow steel tubes. Each pile had a length of 1000 mm, an outer diameter of 89 mm, and a wall thickness of 4 mm. The pile bases were welded to the bottom plate of the model box to reproduce a fixed-end condition. The material properties of the soil and model piles are listed in Table 1. The schematic layout of the model slope and the representative loading process are shown in Fig. 1a,b, respectively.

Table 1: Material properties used in the physical model test.

Material	Density (g/cm^3)	Cohesion (kPa)	Friction Angle (°)	Elastic Modulus (MPa)	Poisson's Ratio
Soil	1.62	5	36.8	35	0.3
Anti-slide pile	7.85	—	—	206,000	0.3

2.2 Instrumentation and Loading Procedure

A displacement-controlled loading scheme was adopted to reproduce the progressive increase in landslide thrust acting on the pile-reinforced slope. A vertical displacement was applied to the slope crest through a rigid loading plate. The loading was conducted in 12 increments, with a displacement increment of 5 mm for each step, resulting in a total applied displacement of 60 mm. After each loading step, data were recorded once the internal stress and deformation of the model had reached a relatively stable state.

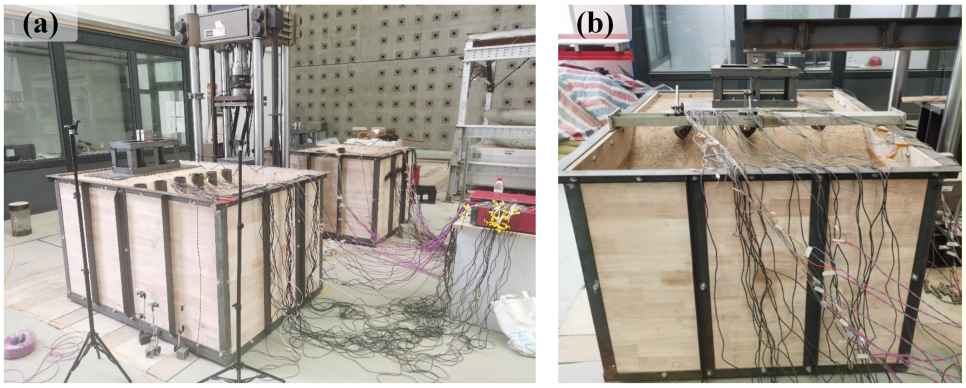


Figure 1: Physical model test configuration: (**a**) Schematic layout of the model slope; (**b**) Representative loading process.

Earth pressure cells and electrical resistance strain gauges were used to monitor the soil pressure response and pile deformation, respectively. To capture the spatial characteristics of the three-dimensional soil arching effect, earth pressure cells were installed behind the anti-slide piles. The cells covered the longitudinal, transverse, and depth directions of the model box. The pressure cells were placed in both the pile-back and pile-between regions. In the vertical direction, three burial depths of 200, 350, and 500 mm were considered. In the horizontal direction, the measuring points were located at distances of 50 and 100 mm from the pile shaft. This arrangement captured spatial variations in earth pressure behind the piles.

The bending response of the model piles was measured using electrical resistance strain gauges. The strain gauges were symmetrically attached to the front and rear sides of each pile along the pile length. Starting from a height of 350 mm above the pile base, five measurement points were arranged at intervals of 100 mm on each side. Thus, each pile had ten strain measurement points. The geometric dimensions of the model slope and the pile arrangement are shown in Fig. 2a, while the plan-view layout of the earth pressure cells is shown in Fig. 2b. The coordinate origin was defined at the midpoint between the two adjacent piles.

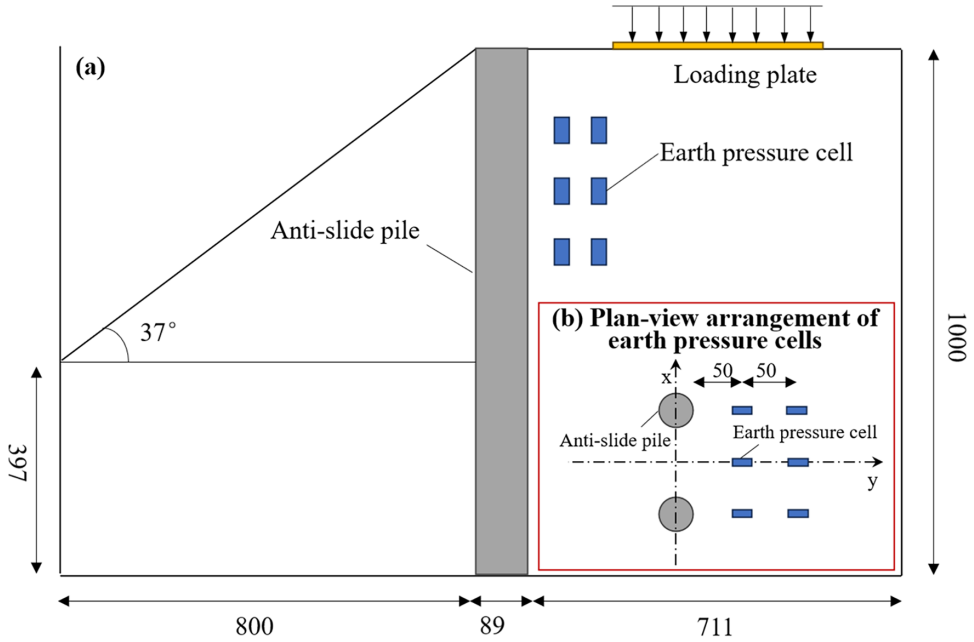


Figure 2: Geometry and instrumentation layout of the physical model: (**a**) Model dimensions and pile arrangement; (**b**) Plan-view layout of earth pressure cells.

2.3 Experimental Observations

Physical model tests were conducted for two pile-spacing ratios, namely s/D = 3 and s/D = 5. For each test, data were recorded after the deformation and earth pressure responses became stable at each loading step. The loading process was terminated when the imposed vertical displacement reached 60 mm. No global slope failure was observed in either case, indicating that the stabilizing piles provided effective resistance against progressive slope movement within the applied loading range. The tests were designed to isolate the effect of pile spacing; soil strength and pile diameter were therefore held constant. Consequently, the experimental observations establish spacing-dependent trends rather than a comprehensive validation across different soils and pile geometries.

For the case of s/D = 3, a clear arch-shaped cracking pattern was observed on the slope surface, as shown in Fig. 3. This pattern indicates that the soil between adjacent piles was strongly constrained by the piles and that the sliding-induced load was redistributed within the pile–soil system. Compared with the larger pile spacing, the smaller spacing promoted stronger interaction between adjacent piles and facilitated the development of a soil arching effect.

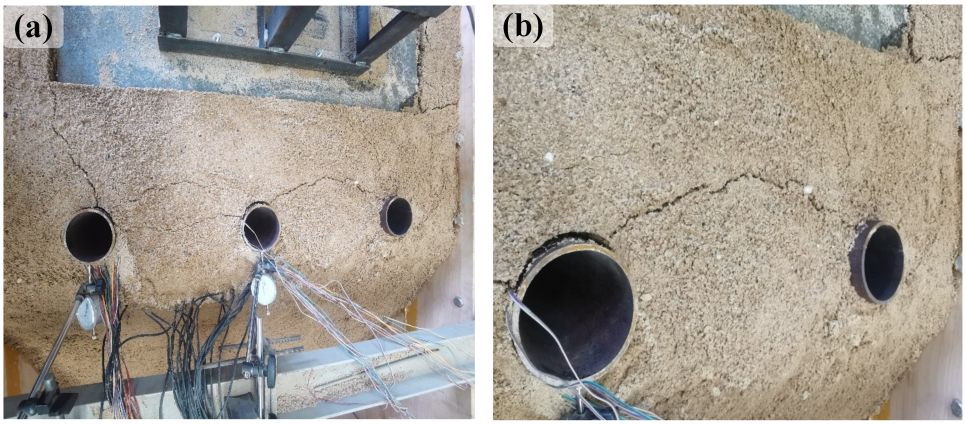


Figure 3: Surface cracking pattern of the slope for s/D = 3: (**a**) Overall view; (**b**) Local enlarged view.

The bending response of the model piles was evaluated based on the measured strains. According to elementary beam theory, the bending moment of the pile can be calculated as:

$$M = \frac{EI\Delta\varepsilon}{D} \tag{1}$$

where E is the elastic modulus of the model pile, I is the second moment of area of the pile section, $\Delta\varepsilon$ is the strain difference between the front and rear sides of the pile, and D is the outer diameter of the hollow circular pile. The second moment of area of the hollow circular section is given by:

$$I = \frac{\pi}{64}\left(D^4 - d^4\right) \tag{2}$$

where d is the inner diameter of the model pile. The strain responses and the corresponding bending moment distributions are shown in Figs. 4 and 5, respectively.

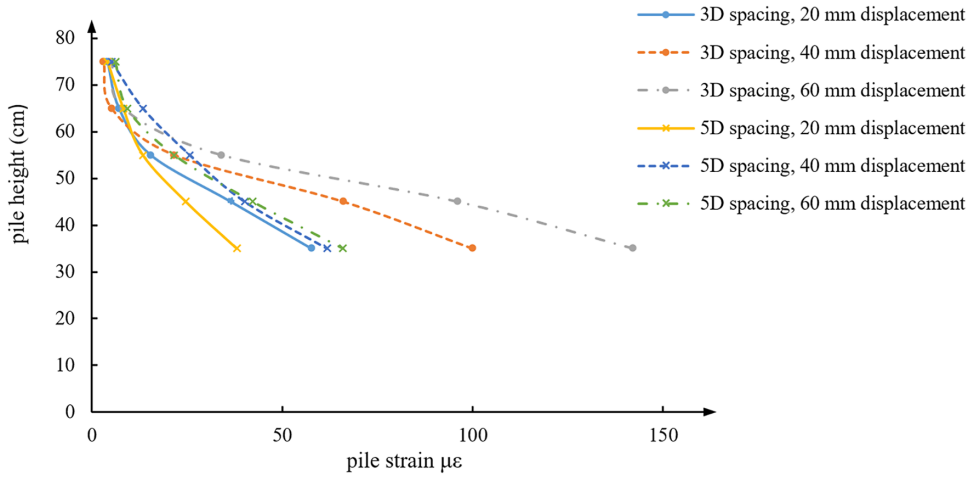


Figure 4: Strain distribution along the model pile under different loading displacements.

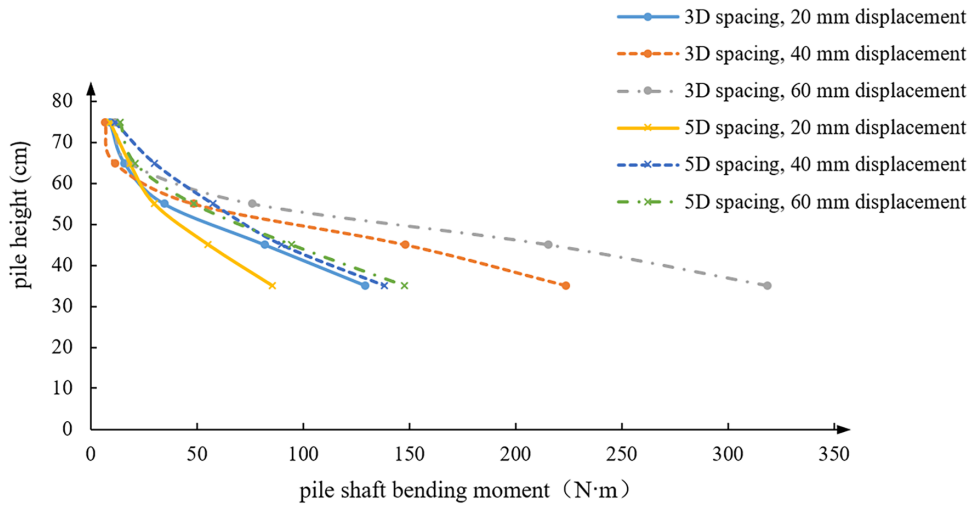


Figure 5: Bending moment distribution along the model pile under different loading displacements.

For both pile-spacing ratios, the pile strain and bending moment increased gradually as the loading displacement increased from 20 to 40 mm and 60 mm. The bending moment was relatively small in the upper part of the pile and increased toward the lower part. This pattern identified the middle-to-lower portion as the primary load-bearing region during slope deformation. Under the same loading displacement, the pile response in the s/D = 3 case was generally greater than that in the s/D = 5 case, particularly at larger loading displacements. These results suggest that a smaller pile spacing enhances the constraint on the inter-pile soil and promotes load transfer from the sliding soil mass to the piles. In contrast, the larger pile spacing weakens the interaction between adjacent piles and reduces the mobilization of the soil arching effect.

The earth pressure distributions behind the piles are shown in Figs. 6 and 7. For s/D = 3, the earth pressure reached a maximum near the central axis between adjacent piles and decreased toward both sides, showing an approximately symmetric distribution. This distribution suggests that the soil between adjacent piles participated in the formation of an arching load-transfer mechanism. Earth pressure concentrations

were more pronounced at locations closer to the piles and at greater burial depths. This trend reflects pile restraint and the increase in sliding thrust with depth.

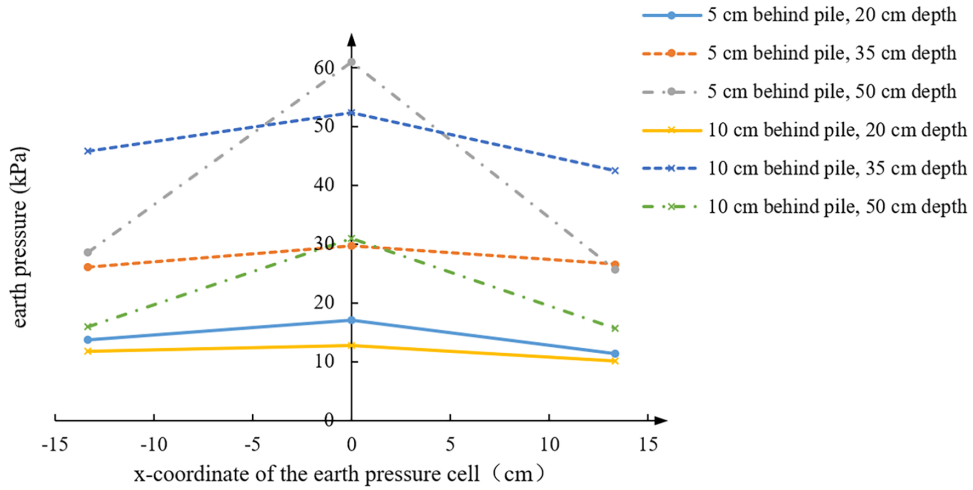


Figure 6: Earth pressure distributions behind the piles under $s/D = 3$.

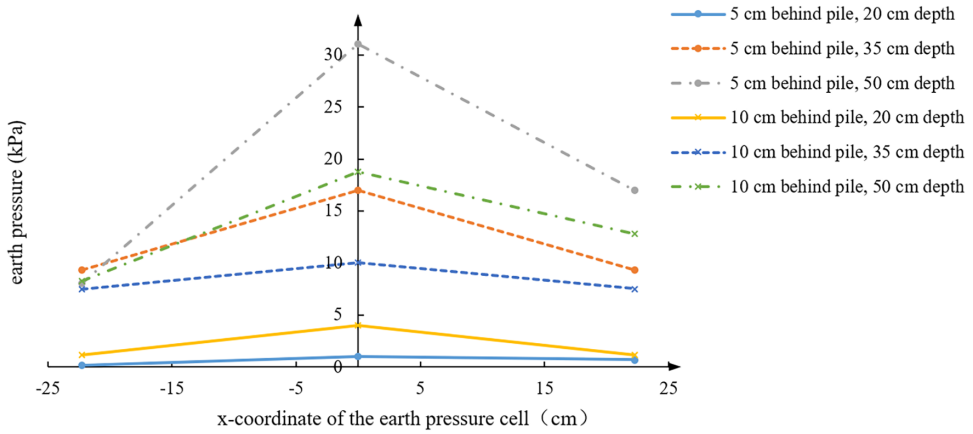


Figure 7: Earth pressure distributions behind the piles under $s/D = 5$.

Compared with $s/D = 3$, the earth pressure distribution in the $s/D = 5$ case was more uniform, and the stress concentration near the inter-pile region was less evident. This indicates that increasing the pile spacing weakens the cooperative constraint between adjacent piles and reduces the degree of soil arching. Overall, pile spacing strongly affected soil arching, earth-pressure distribution, and pile bending. These observations provide a physical basis for the subsequent finite element validation and safety factor database construction.

3 Finite Element Modelling and Database Construction

3.1 Parameterized Three-Dimensional FEM Model

A parameterized three-dimensional finite element model was established to simulate the stability of pile-reinforced slopes and to generate the numerical database for subsequent machine-learning analysis. The model represents a single-row anti-slide pile system embedded in a slope. The slope geometry, pile diameter,

pile spacing, and pile position were defined as controllable modelling parameters, allowing the model to be automatically updated for different design cases [32,33].

To reduce the computational cost, the symmetry of the single-row pile arrangement was considered in the numerical model. A representative soil domain containing two half piles was adopted, and normal displacement constraints were applied on the symmetry planes. The model width was kept consistent with the spacing between two adjacent pile centers. This treatment enabled the three-dimensional pile–soil interaction to be represented while maintaining a moderate computational scale [34]. The slope soil was described using a Mohr–Coulomb elastoplastic model, while the anti-slide piles were modelled as linear elastic materials. The interaction between the piles and the surrounding soil was simulated using hard contact in the normal direction and a penalty friction formulation in the tangential direction. The friction coefficient was defined as $\mu = \tan(0.75\varphi)$, where φ is the soil friction angle [35,36]. The soil and pile domains were discretized using C3D8 elements, and local mesh refinement was applied near the pile–soil interface to improve the representation of stress transfer.

The boundary conditions were defined to represent the constraint of the soil domain and the embedded pile system. Normal displacement constraints were applied to the lateral boundaries of the soil domain, while the bottom of the soil and piles was fixed. Gravity loading was applied according to the unit weights of the soil and pile materials. Based on this modelling framework, a cohesion anisotropy formulation was further introduced to account for the directional strength characteristics of natural sedimentary soils, as described in the following section.

3.2 Implementation of Cohesion Anisotropy

Natural sedimentary soils often exhibit directional strength characteristics owing to deposition-induced particle orientation [37]. Since the mobilized shear strength of soil is closely related to the principal stress direction, the strength parameters may vary under different stress states. Previous studies have shown that cohesion is more sensitive to strength anisotropy than the friction angle [9]. Accordingly, the friction angle was held constant. Cohesion varied with the major principal-stress direction to represent soil-strength anisotropy.

In the Mohr–Coulomb criterion, the shear strength of soil is governed by cohesion c and friction angle φ. When cohesion anisotropy is considered, the cohesion at an integration point is assumed to depend on the angle between the major principal stress direction and the vertical deposition direction. The anisotropic cohesion is expressed as

$$c_\theta = c_h + (c_v - c_h)\cos^2\theta \tag{3}$$

where c_θ is the direction-dependent cohesion, c_h is the horizontal cohesion, c_v is the vertical cohesion along the deposition direction, and θ is the angle between the major principal stress direction and the vertical direction. When $\theta = 0$, the major principal stress direction is aligned with the deposition direction and $c_\theta = c_v$. When $\theta = \pi/2$, $c_\theta = c_h$.

The cohesion anisotropy coefficient is defined as:

$$k = \frac{c_h}{c_v} \tag{4}$$

Thus, Eq. (3) can be rewritten as:

$$c_\theta = c_v\left(k + (1-k)\cos^2\theta\right) \tag{5}$$

when $k = 1$, $c_\theta = c_h = c_v$, and the model degenerates into an isotropic cohesion model. In this study, $k = 0.7$ was adopted to represent a moderate degree of cohesion anisotropy in natural sedimentary soils. This value is a modelling assumption rather than a site-calibrated parameter. Because an independent sensitivity analysis of k was not included in the present database, the resulting safety factors should be interpreted for the specified anisotropy level; extending the framework to other depositional fabrics requires recalibration or a dedicated sensitivity study.

For a two-dimensional stress state, the major principal stress direction can be determined from the current stress components. Considering the horizontal stress σ_x, vertical stress σ_y, and shear stress τ_{xy}, the following relationship can be obtained:

$$\cos 2\theta = \frac{\sigma_y - \sigma_x}{2R} \tag{6}$$

where

$$R = \sqrt{\left(\frac{\sigma_y - \sigma_x}{2}\right)^2 + \tau_{xy}^2} \tag{7}$$

For the three-dimensional slope problem, the soil was assumed to be transversely anisotropic, with the vertical direction taken as the deposition direction [37]. Two orthogonal vertical planes were considered, namely the xy and yz planes. The corresponding values of $\cos^2\theta$ were calculated from the stress components in these two planes, and the larger value was selected as the controlling directional parameter:

$$\cos^2\theta = \max\left(\cos^2\theta_{xy}, \cos^2\theta_{yz}\right) \tag{8}$$

The cohesion anisotropy model was implemented in ABAQUS using the USDFLD user subroutine. At each material integration point, the current stress components were retrieved, and the directional parameter $\cos^2\theta$ was calculated based on the local principal stress direction. This parameter was then assigned as a field variable. Since the cohesion varies linearly with $\cos^2\theta$, the cohesion value was updated through the predefined field-dependent material properties during the finite element analysis. In this way, the shear strength of the soil could be dynamically adjusted according to the evolving stress direction.

3.3 Validation against Physical Model Tests

To evaluate the finite element modelling approach under the tested configuration, a numerical model corresponding to the physical model test with $s/D = 3$ was established. The geometric dimensions, material parameters, boundary conditions, and loading scheme were kept consistent with those used in the physical test. Wang and Jin [38] reported that cohesion anisotropy coefficient generally ranges from 0.5 to 1.0, with $k = 1.0$ representing isotropic strength, and adopted $k = 0.7$ as a representative intermediate condition. Their sensitivity results showed that the influence of k depends on slope geometry and cohesion level. For example, for a gentle slope with $c_v = 47.88$ kPa, the calculated safety factors were 1.51, 1.59, and 1.71 for $k = 0.5$, 0.7, and 1.0, respectively, whereas the corresponding influence was smaller for a steep slope. Based on this published evidence, $k = 0.7$ was adopted in the present study as a representative moderate anisotropy level rather than a universally optimal or site-calibrated value. The validation model is shown in Fig. 8.

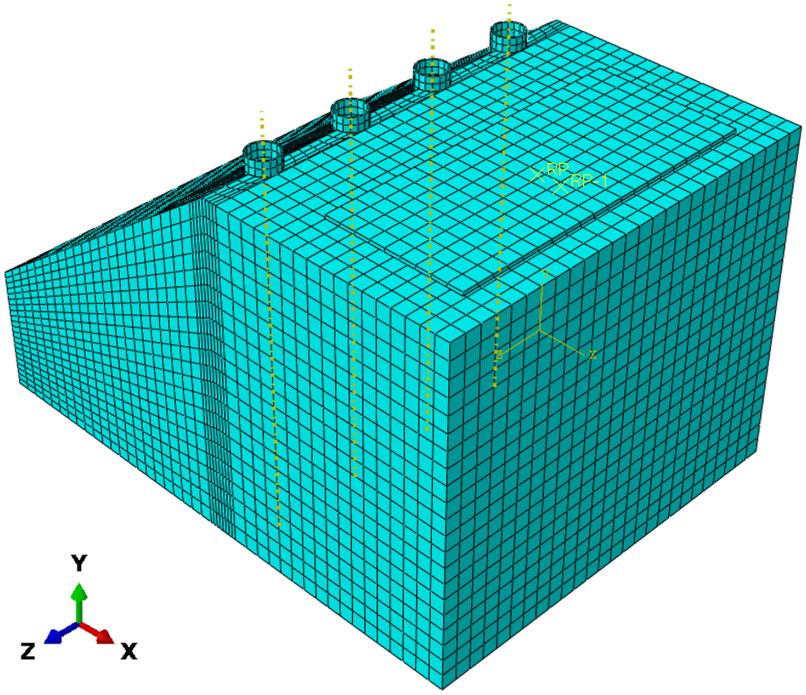


Figure 8: Finite element model for the validation case with a pile-spacing ratio of $s/D = 3$.

In the numerical model, the loading plate was simulated as a rigid body. A reference point was defined at the center of the loading plate and coupled with the plate to impose displacement-controlled loading. The bottom of the slope and the pile bases were fixed to reproduce the boundary constraint of the model box and the welded pile bases in the experiment. Normal displacement constraints were applied to the side boundaries of the soil domain. The analysis comprised 13 steps. The first step was used to establish the initial stress state under self-weight, followed by 12 loading steps with a vertical displacement increment of 5 mm, giving a final displacement of 60 mm.

The overall displacement magnitude of the numerical model at the final loading stage is shown in Fig. 9. The displacement was mainly concentrated near the loading plate and gradually propagated toward the interior of the slope. When the deformation developed toward the pile-reinforced region, the displacement magnitude was significantly reduced owing to the restraining effect of the anti-slide piles. No continuous failure surface was formed at the final loading stage, which is consistent with the physical model observations.

Fig. 10 further compares the displacement contours of the slope under the self-weight and final top-loading conditions. Under self-weight, the slope deformation was relatively small and was mainly governed by settlement. After the top loading was applied, the displacement field developed from the crest region toward the slope body, while the displacement contours became denser around the pile-reinforced zone. This indicates that the piles effectively limited the downslope movement of the soil and altered the deformation path of the slope.

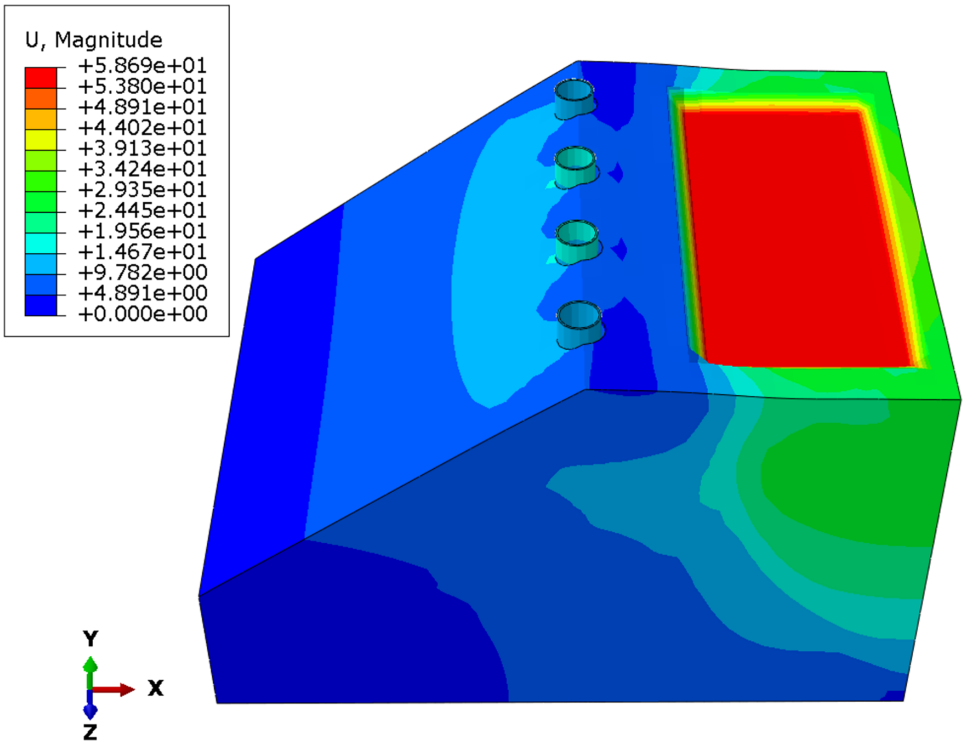


Figure 9: Overall displacement magnitude of the finite element model at the final loading stage.

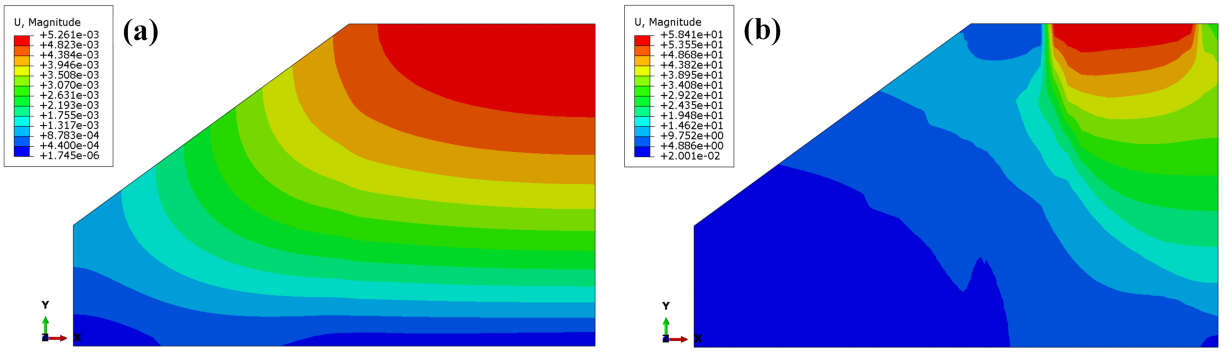


Figure 10: Displacement contours of the slope under different loading conditions: (**a**) Self-weight condition; (**b**) Top-loading condition.

The evolution of the maximum principal stress under different loading displacements is shown in Fig. 11. At a loading displacement of 20 mm, the stress redistribution around the piles was still limited. As the displacement increased to 40 mm, a distinct arch-shaped stress zone began to develop between adjacent piles, suggesting the initial formation of a soil arching mechanism. When the displacement reached 60 mm, the arch-shaped stress region became more pronounced and extended between adjacent piles. This development indicates that the sliding-induced load was progressively transferred through the inter-pile soil to the piles. This stress redistribution pattern is consistent with the earth pressure distribution observed in the physical model tests.

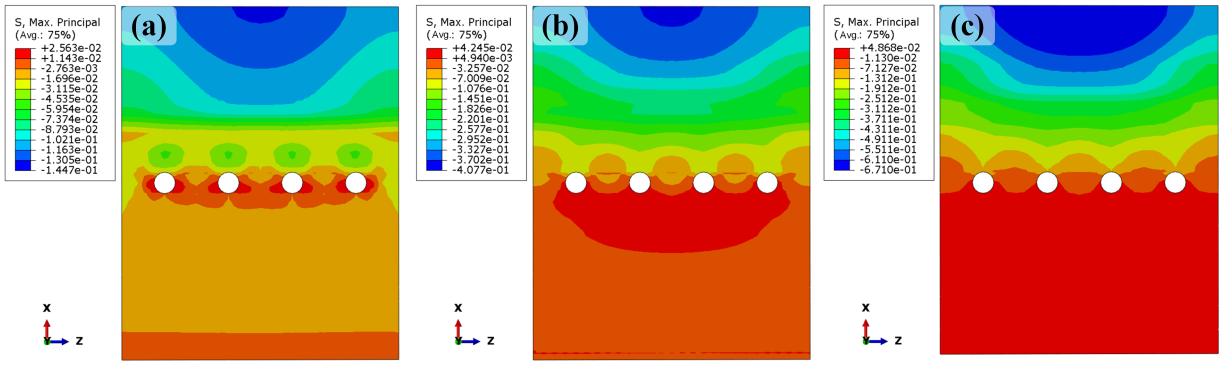


Figure 11: Maximum principal stress contours showing the evolution of the soil arching effect between anti-slide piles under different loading displacements: (**a**) 20 mm; (**b**) 40 mm; (**c**) 60 mm.

The bending moment distribution along the pile shaft is presented in Fig. 12. The bending moment increased with the applied displacement, and the relatively large bending moment mainly occurred in the middle-to-lower portion of the pile. This trend agrees with the experimental results, indicating that the finite element model captures the main load-bearing region of the anti-slide pile under progressive slope deformation.

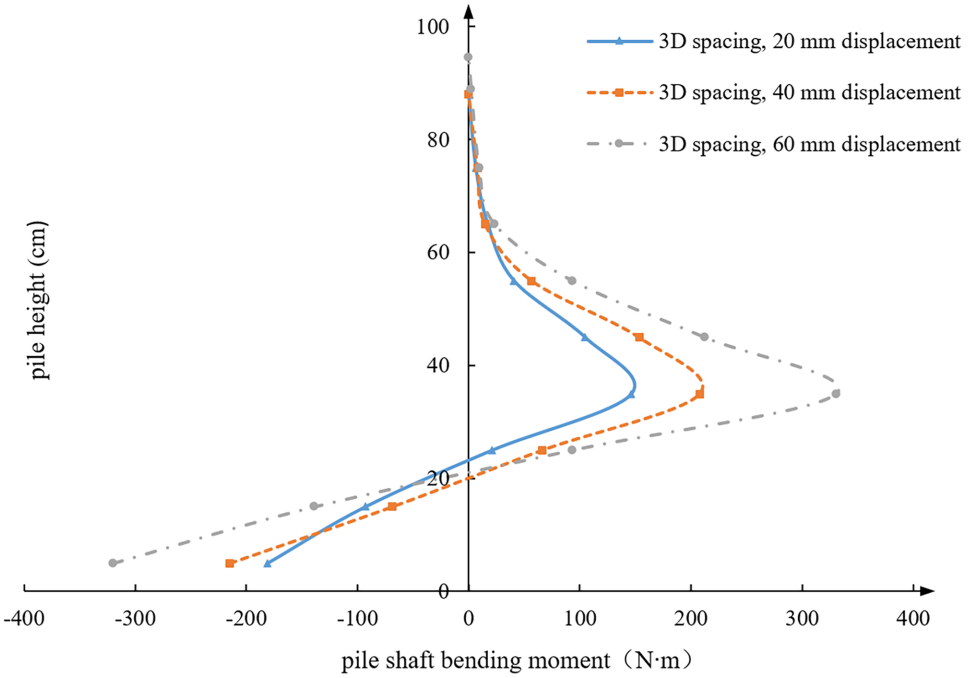


Figure 12: Simulated bending moment distribution along the pile shaft under different loading displacements.

Since the strain gauges in the physical model test covered only part of the pile length, the simulated bending moments were extracted at the same measurement heights for quantitative comparison. The comparison results are listed in Table 2. The average absolute relative errors were 19.39%, 15.53%, and 13.83% for loading displacements of 20, 40, and 60 mm, respectively, giving an overall average of approximately 16.25%. Some relatively large percentage errors occurred in the upper part of the pile, where the measured bending moments were small. For example, the relative errors at a pile height of 75 cm under 20 mm

loading and at 65 cm under 40 mm loading were 29.14% and 28.34%, respectively, whereas the corresponding absolute differences were only 2.69 and 3.27 N·m. Larger local relative errors occurred where the measured bending moments were small and therefore more sensitive to modest absolute differences. Additional discrepancies may arise from the idealized model-box boundaries, the fixed pile-base representation, the Mohr–Coulomb soil idealization, and uncertainty in pile–soil contact parameters. Thus, the validation supports the overall response pattern and load-bearing region, but does not imply pointwise agreement at every measurement location.

Table 2: Comparison between simulated and experimental pile bending moments.

Loading Level	Pile Height (cm)	35	45	55	65	75
20 mm loading displacement	Experimental moment (N·m)	129.20	81.83	34.61	15.95	9.23
	Simulated moment (N·m)	146.35	104.84	40.84	17.29	6.54
	Relative error	13.27%	28.12%	18.00%	8.40%	−29.14%
	Absolute error (N·m)	17.15	23.01	6.23	1.34	2.69
40 mm loading displacement	Experimental moment (N·m)	223.80	148.00	48.45	11.54	6.92
	Simulated moment (N·m)	208.50	153.30	56.71	14.81	8.43
	Relative error	−6.84%	3.58%	17.05%	28.34%	21.82%
	Absolute error (N·m)	15.30	5.30	8.26	3.27	1.51
60 mm loading displacement	Experimental moment (N·m)	318.39	215.24	76.13	18.45	11.54
	Simulated moment (N·m)	330.8	212.40	93.24	23.38	9.838
	Relative error	3.90%	−1.32%	22.47%	26.72%	−14.75%
	Absolute error (N·m)	12.41	2.84	17.11	4.93	1.70

Taken together, the finite element model reproduced three principal response characteristics observed in the physical test: the absence of a continuous surface failure, the progressive development of the inter-pile stress-arching pattern, and the variation and dominant region of pile bending. The quantitative comparison included 15 paired bending-moment values covering three loading displacements and five elevations along the pile. The mean absolute relative errors were 19.39%, 15.53%, and 13.83% at loading displacements of 20, 40, and 60 mm, respectively, with an overall average of 16.25%. The consistency obtained across different loading stages and pile elevations, together with the qualitative agreement in deformation and soil-arching patterns, further supports the conclusion that, under the investigated test condition, the adopted FEM provides a reasonable representation of the principal pile–soil interaction response.

3.4 Strength Reduction Analysis and Database Generation

The finite element strength reduction method was adopted to calculate the safety factor of pile-reinforced slopes. For each numerical case, the initial geostatic equilibrium was first established under self-weight. Subsequently, the soil strength parameters were reduced simultaneously using a strength reduction factor F_r. The reduced cohesion and friction angle were calculated as:

$$c_m = \frac{c}{F_r} \tag{9}$$

$$\varphi_m = \arctan\left(\frac{\tan\varphi}{F_r}\right) \tag{10}$$

where F_r is the strength reduction factor, c_m and φ_m are the original cohesion and friction angle, respectively. The c_F and φ_F are the reduced cohesion and friction angle, respectively. Since the cohesion anisotropy model was implemented through the USDFLD subroutine, the field-dependent cohesion parameters were updated automatically using a Python-based preprocessing script during the strength reduction analysis.

A bisection search strategy was used to determine the critical reduction factor. For each trial value of F_r, a finite element analysis was performed to evaluate the stability state of the slope. Numerical non-convergence was adopted as the failure criterion. The search stopped when the difference between the bounds was below 0.01. The corresponding critical reduction factor was defined as the slope safety factor, *FS*. For the baseline case, the calculated *FS* was 2.078.

Representative cases provided a preliminary assessment of the key parameters. Pile spacing, soil cohesion, and friction angle were varied individually, while all other parameters remained fixed. The results are summarized in Table 3. As the pile spacing increased from 2 to 4 m, *FS* decreased from 2.218 to 1.962. Thus, wider pile spacing weakened inter-pile restraint and reduced soil arching. In contrast, increasing the cohesion from 15 to 35 kPa increased *FS* from 1.640 to 2.500, while increasing the friction angle from 15° to 35° increased *FS* from 1.593 to 2.546. These results confirm that the stability of pile-reinforced slopes is jointly controlled by soil strength parameters and pile layout, which supports their selection as input variables for subsequent machine-learning prediction.

Table 3: Safety factors of pile-reinforced slopes under different parameter variations.

Parameter Group	Cohesion (kPa)	Friction Angle (°)	Pile Spacing (m)	*FS*
Pile spacing variation	25	25	2	2.218
	25	25	3	2.078
	25	25	4	1.962
Cohesion variation	15	25	3	1.640
	25	25	3	2.078
	35	25	3	2.500
Friction angle variation	25	15	3	1.593
	25	25	3	2.078
	25	35	3	2.546

To generate a numerical database for machine-learning-based *FS* prediction, an automated FEM workflow was developed. The workflow consisted of four main steps: parameter sampling, automatic model generation, batch strength reduction analysis, and result extraction. In this framework, the finite element model was automatically updated according to the sampled input parameters, and the corresponding *FS* was calculated using the strength reduction procedure described above.

The input parameter space was sampled using a Sobol low-discrepancy sequence. Compared with conventional random sampling, Sobol sampling reduces sample clustering and provides progressively more uniform coverage of a bounded multidimensional domain. Six input variables were considered: soil unit weight γ, cohesion c, friction angle φ, pile position x_p, pile diameter D, and spacing ratio s/D. The pile spacing s was calculated from the sampled pile diameter and spacing ratio. The parameter ranges (Table 4) were not derived from a specific case history or design code. They were deliberately selected as broad, physically feasible intervals to cover diverse soil properties and pile layouts. These ranges define the applicability domain of the present surrogate model rather than universal design limits.

Table 4: Statistical characteristics of variables in the pile-reinforced slope database.

Features			Statistical Characteristics			
Variable Type	**Symbol**	**Description**	**Mean**	**Standard Deviation**	**Min**	**Max**
Input	γ	Unit weight (kN/m^3)	20.5	2.022	17.011	23.999
Input	c	Cohesion (kPa)	25.0	8.664	10.017	39.978
Input	φ	Friction angle (°)	25.0	8.664	10.022	39.972
Input	x_p	Pile position (m)	7.5	3.177	2.002	13.000
Input	D	Pile diameter (m)	1.7	0.404	1.000	2.400
Input	s/D	Spacing ratio	4.0	1.155	2.004	6.000
Output	FS	Safety factor	1.6	0.532	0.300	3.000

To quantitatively evaluate the space-filling quality of the Sobol samples, the six input variables were first normalized to the unit hypercube according to their prescribed lower and upper bounds. The centered discrepancy was then calculated for nested Sobol subsets containing 64, 128, 256, 512, and 1024 samples. Smaller discrepancy values indicate a more uniform distribution of sampling points within the multidimensional parameter space. Powers-of-two sample sizes were selected to preserve the balance properties of the Sobol sequence.

As shown in Fig. 13, the centered discrepancy decreased monotonically as the number of Sobol samples increased. The discrepancy values were 5.319×10^{-3}, 1.592×10^{-3}, 5.497×10^{-4}, 1.781×10^{-4}, and 6.120×10^{-5} for 64, 128, 256, 512, and 1024 samples, respectively. From 64 to 1024 samples, the centered discrepancy decreased by approximately 98.85%, demonstrating a substantial improvement in the uniformity of coverage of the six-dimensional input domain. The reduction remained evident when the sample size increased from 512 to 1024, supporting the use of 1024 samples from the perspective of parameter-space coverage.

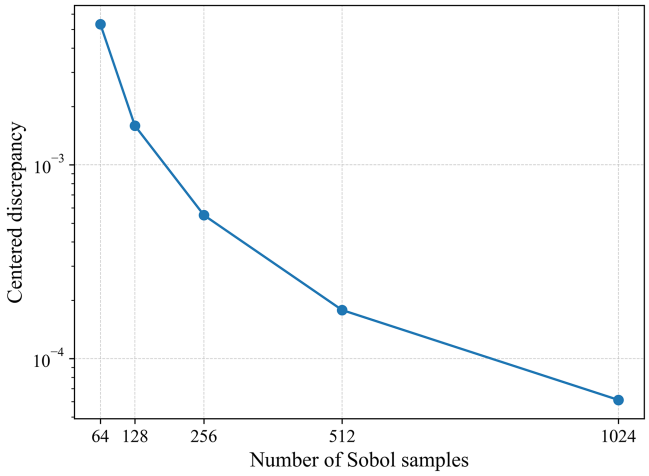


Figure 13: Centered discrepancy of nested Sobol sample sets in the normalized six-dimensional input space.

A total of 1024 (2^{10}) finite element cases were therefore generated using the Sobol sequence. After each strength-reduction analysis, the calculated FS, solution status, and diagnostic information were automatically extracted and stored in structured CSV files. The individual files were subsequently merged and sorted according to the sample index to form the final finite element database. The centered-discrepancy analysis

evaluates only the coverage of the input parameter space. The adequacy of the database for machine-learning training is examined separately through the KAN database-size sensitivity analysis presented in Section 4.5.

3.5 Sensitivity Analysis of Anisotropic Coefficient k

In the present study, the anisotropic strength coefficient k was adopted as 0.7 during FEM database generation based on previous investigations of soil strength anisotropy [38]. Although previous studies have reported that the anisotropic coefficient generally ranges from 0.5 to 1.0, the slope configurations and reinforcement conditions considered therein are different from those investigated in this study. Therefore, a sensitivity analysis was performed to examine whether the selection of k influences the generated FS labels and the subsequent data-driven analysis.

After completing the FEM database, three representative cases were selected from the FEM database according to their FS values (Table 5), including a marginally stable case, a medium-stability case, and a highly stable case. These cases cover different stability states within the generated database. Keeping all other geometric and material parameters unchanged, additional FEM strength-reduction analyses were conducted by assigning k = 0.5, 0.7, and 1.0. The corresponding FS values and relative variations are summarized in Table 6.

Table 5: Representative cases selected from FEM database.

Case	γ (kN/m^3)	c (kPa)	φ (°)	x (m)	D (m)	s/D
Case 1 (ID12)	20.3469	15.3514	19.2551	3.3468	2.0979	4.2915
Case 2 (ID2)	21.8579	16.8791	30.5641	4.3969	2.0355	3.5953
Case 3 (ID1)	17.3727	39.3724	23.6599	8.8362	1.2757	4.0254

Table 6: Sensitivity of FS to k.

Case	$FS_{k=0.7}$	$FS_{k=0.5}$	$\Delta FS_{k=0.5}$	$FS_{k=1.0}$	$\Delta FS_{k=1.0}$
Case 1	0.975	0.910	−6.70%	1.070	9.70%
Case 2	1.297	1.240	−4.40%	1.380	6.40%
Case 3	2.453	2.249	−8.30%	2.701	10.10%

As shown in Table 6, increasing k from 0.5 to 1.0 increases the calculated FS because a higher k value corresponds to a weaker degree of cohesion anisotropy and therefore a higher mobilized soil strength. Relative to the baseline results at k = 0.7, decreasing k to 0.5 changes FS by −8.3% to −4.4%, whereas increasing k to 1.0 changes FS by +6.4% to +10.1%. Although the absolute FS values vary with k, the three cases retain the same relative stability ordering. Since the variation induced by k is within a limited range and does not alter the relative stability trend, the selected k = 0.7 provides a reasonable representation for constructing the FEM database. Accordingly, k = 0.7 was retained as a representative intermediate value for database construction. The consistent response direction and unchanged stability ordering provide supporting evidence that the qualitative data-driven interpretation is unlikely to be dominated by the selected k within the examined range.

4 Machine Learning-Based Safety Factor Prediction

Based on the finite element database constructed in Section 3, a machine-learning-based framework was developed for rapid FS prediction of pile-reinforced slopes. As shown in Fig. 14, the overall workflow consists of data representation and preprocessing, training–test splitting, cross-validation-based hyperparameter optimization, comparative evaluation of multiple machine-learning models, and SHAP-based interpretability analysis. The trained models captured the nonlinear relationship between soil–pile parameters and the slope safety factor. SHAP analysis [29,39] quantified the contributions of the input variables.

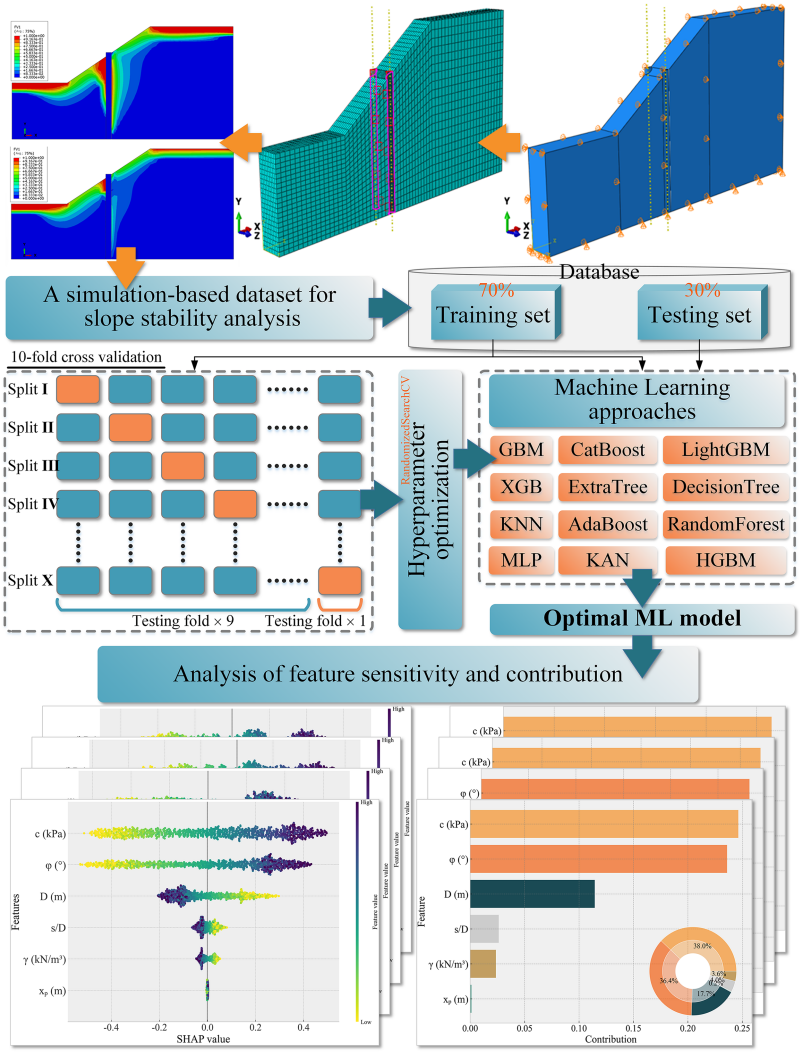


Figure 14: Data-driven framework for machine-learning-based *FS* prediction and SHAP-based interpretability analysis.

4.1 Data Representation and Preprocessing

The finite element database generated in Section 3.4 was used to develop machine-learning models for rapid safety factor prediction of pile-reinforced slopes. Each numerical sample was represented by a tabular input–output pair [40]. The input vector consisted of six variables, including the soil unit weight γ, cohesion c, friction angle φ, pile position x_p, pile diameter D, and spacing ratio s/D. The corresponding output was the safety factor, denoted as FS, obtained from the finite element strength reduction method.

For the i-th sample, the input vector can be expressed as:

$$\mathbf{x}_i = \left[\gamma_i, c_i, \varphi_i, x_{p,i}, D_i, (s/D)_i\right] \tag{11}$$

and the corresponding target value is

$$y_i = FS_i \tag{12}$$

where $\mathbf{x}_i$ is the input feature vector and y_i is the FEM-derived safety factor.

Before model training, all samples were checked to ensure that the finite element analyses were successfully completed and that the extracted *FS* values were valid. The database was then divided into training and test sets [41]. The training set was used for model fitting and hyperparameter selection, whereas the test set was retained for evaluating the generalization performance of the trained models [15]. Since the six input variables have different physical units and numerical ranges, feature standardization was applied before model training [16].

For each input variable, the standardized value was calculated as:

$$\tilde{x}_{ij} = \frac{x_{ij} - \mu_j}{\sigma_j} \tag{13}$$

where x_{ij} is the original value of the j-th feature in the i-th sample, and μ_j and σ_j are the mean and standard deviation of the j-th feature, respectively. To avoid data leakage, μ_j and σ_j were calculated only from the training set and then applied to both the training and test sets. The target variable *FS* was kept in its original physical scale for model evaluation.

The standardized input features and FEM-derived *FS* values were then used to train and compare different machine-learning models. This data representation enabled the nonlinear relationship between soil parameters, pile layout characteristics, and slope stability to be learned directly from the finite element database.

4.2 Machine Learning Models and Evaluation Metrics

To establish a reliable data-driven mapping between the input parameters and FS, a library of twelve machine-learning algorithms was developed and evaluated [14], as illustrated in Fig. 14. The selected models cover representative regression strategies, including tree-based ensemble learning, single-tree learning, instance-based learning, and neural-network-based learning. The model categories and corresponding algorithms are summarized in Table 7. This model library enables a systematic comparison of different nonlinear regression approaches for *FS* prediction of pile-reinforced slopes.

Table 7: Machine-learning models used for *FS* prediction.

Model Category	Models	Role
Tree-based ensemble models [14]	AdaBoost, CatBoost, GBM, HGBM, LightGBM, Random Forest, XGB	Nonlinear regression and feature interaction learning
Single-tree models [14]	DecisionTree, ExtraTree	Baseline tree models
Instance-based model	KNN	Local similarity-based prediction
Neural-network-based models [28,42,43]	MLP, KAN	Nonlinear function approximation

The finite element database was divided into a training set and an independent test set with a ratio of 7:3 [44]. The training set was used for model fitting and hyperparameter optimization, whereas the test set was used only for the final evaluation of generalization performance. To improve model robustness and reduce the influence of a single data split during hyperparameter selection, 10-fold cross-validation was performed on the training set [45]. In each cross-validation iteration, nine folds were used for training and the remaining fold was used for validation [22]. The optimal hyperparameter combination was determined using RandomizedSearchCV [21], and the final model was retrained on the complete training set before being evaluated on the independent test set [46].

Model performance was evaluated using five regression metrics: the coefficient of determination R^2 [13,23], mean squared error (MSE) [47], root mean squared error (RMSE), mean absolute error (MAE) [16], and mean absolute percentage error (MAPE) [48]. These metrics are defined as follows:

$$R^2 = 1 - \frac{\sum_{i=1}^{n} (y_i - \hat{y}_i)^2}{\sum_{i=1}^{n} (y_i - \overline{y})^2} \tag{14}$$

$$\mathrm{MSE} = \frac{1}{n} \sum_{i=1}^{n} (y_i - \hat{y}_i)^2 \tag{15}$$

$$\mathrm{RMSE} = \sqrt{\frac{1}{n} \sum_{i=1}^{n} (y_i - \hat{y}_i)^2} \tag{16}$$

$$\mathrm{MAE} = \frac{1}{n} \sum_{i=1}^{n} |y_i - \hat{y}_i| \tag{17}$$

$$\mathrm{MAPE} = \frac{1}{n} \sum_{i=1}^{n} \left| \frac{y_i - \hat{y}_i}{y_i} \right| \tag{18}$$

where y_i and $\hat{y}_i$ are the FEM-derived and predicted safety factors of the i-th sample, respectively, $\overline{y}$ is the mean value of the FEM-derived safety factors, and n is the number of evaluated samples. A higher R^2 and lower MSE, RMSE, MAE, and MAPE indicate better prediction accuracy. In addition, the differences between the training and test metrics were analyzed to assess the generalization ability and potential overfitting behavior of each model.

4.3 Comparative Prediction Performance

Table 8 summarizes the prediction performance of the twelve models on the training and test sets, and Fig. 15 visualizes the corresponding metrics. MLP achieved the highest test R^2 (0.928) and the lowest test RMSE (0.138). KAN ranked second in test R^2 (0.913; difference from MLP = 0.015) and RMSE (0.152), while its test MAE (0.084) was slightly lower than that of MLP (0.085); both models had a test MAPE of 0.058. Overall, MLP provided the strongest accuracy-oriented result on the selected test split, whereas KAN showed competitive performance with a slightly lower MAE. These metric differences alone do not establish statistical superiority; therefore, paired statistical comparisons are presented in Section 4.4.

Among the tree-based ensemble models, CatBoost and LightGBM produced relatively stable test performance. CatBoost achieved a test R^2 of 0.889 and RMSE of 0.171, while LightGBM achieved a test R^2 of 0.880 and RMSE of 0.178. HGBM and GBM also showed acceptable predictive performance, with test R^2 values of 0.868 and 0.863, respectively. However, some models exhibited a clear discrepancy between training and test performance. For example, KNN achieved a perfect training R^2 of 1.000, but its test R^2 decreased to 0.858. Similarly, XGB obtained a training R^2 of 0.998, whereas its test R^2 was only 0.840. These results indicate

that excellent fitting performance on the training set does not necessarily guarantee robust prediction on unseen data.

Table 8: Comparison of evaluation metrics for the twelve models on the training and test sets.

Model	R^2		MSE		RMSE		MAE		MAPE	
	Train	Test	Train	Test	Train	Test	Train	Test	Train	Test
AdaBoost	0.977	0.830	0.007	0.045	0.081	0.211	0.066	0.136	0.049	0.092
CatBoost	0.966	0.889	0.010	0.029	0.099	0.171	0.056	0.093	0.043	0.060
DecisionTree	0.792	0.685	0.061	0.083	0.246	0.288	0.165	0.210	0.123	0.138
ExtraTree	0.854	0.829	0.043	0.045	0.206	0.212	0.132	0.141	0.103	0.095
GBM	0.994	0.863	0.002	0.036	0.041	0.190	0.024	0.113	0.019	0.074
HGBM	0.973	0.868	0.008	0.035	0.088	0.186	0.045	0.115	0.037	0.077
KAN	0.930	0.913	0.020	0.023	0.143	0.152	0.074	0.084	0.061	0.058
KNN	1.000	0.858	0.000	0.037	0.000	0.193	0.000	0.134	0.000	0.094
LightGBM	0.952	0.880	0.014	0.032	0.118	0.178	0.064	0.109	0.053	0.074
MLP	0.912	0.928	0.026	0.019	0.160	0.138	0.087	0.085	0.070	0.058
RandomForest	0.976	0.836	0.007	0.043	0.084	0.208	0.053	0.144	0.041	0.096
XGB	0.998	0.840	0.001	0.042	0.022	0.205	0.017	0.128	0.012	0.085

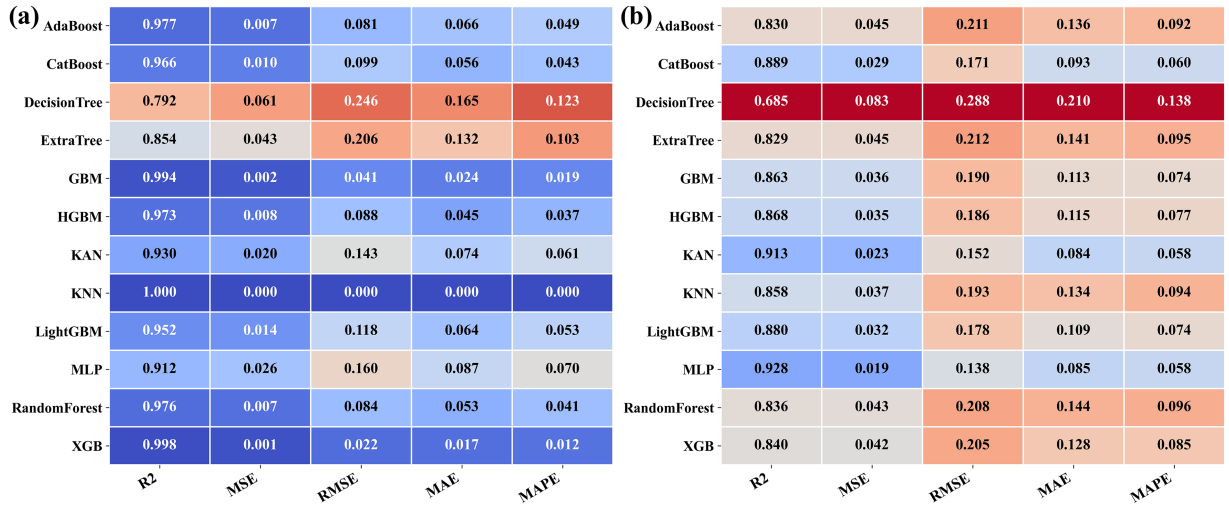


Figure 15: Heatmap comparison of evaluation metrics for the twelve models: (**a**) Training set; (**b**) Test set.

The average-rank-based comparison shown in Fig. 16 further confirms the strong performance of MLP and KAN on the independent test set. Although MLP ranked first with an average rank of 1.30, KAN ranked second with an average rank of 1.70, showing only a small difference from MLP. In contrast, KNN, XGB, and GBM ranked among the best models on the training set but showed lower rankings on the test set. This ranking shift suggests that these models may have learned sample-specific patterns in the training data rather than a generalizable relationship between the input variables and *FS*. Compared with these models, KAN maintained a more balanced performance across the training and test sets, demonstrating its robustness for *FS* prediction of pile-reinforced slopes.

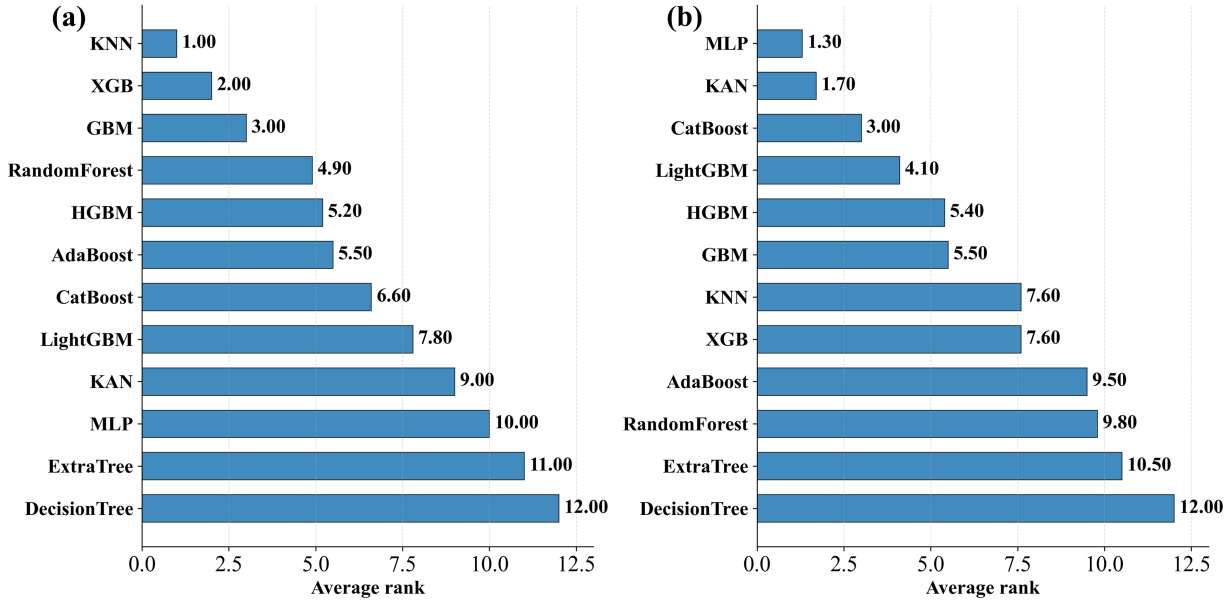


Figure 16: Average-rank-based overall performance comparison of the twelve models: (**a**) Training set; (**b**) Test set.

The train–test performance gaps in terms of R^2 and MSE are shown in Fig. 17. KAN exhibited a small R^2 gap of 0.017 and an MSE gap of 0.003, indicating limited overfitting and stable generalization performance. In comparison, XGB, KNN, AdaBoost, Random Forest, and GBM showed relatively large train–test gaps, despite their high training accuracy. MLP showed the smallest gap, with its test performance slightly better than its training performance. This phenomenon may be related to the data split, regularization effect, or the distribution of samples in the test set. Therefore, although MLP achieved the highest numerical accuracy on the test set, KAN provided a more consistent balance between fitting ability and generalization stability.

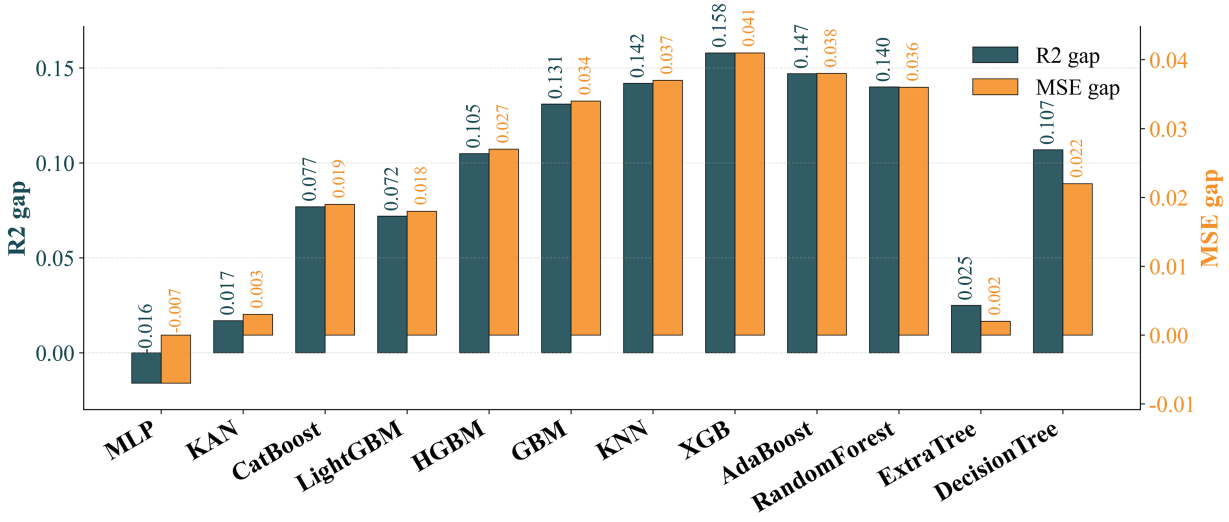


Figure 17: Train-test performance gaps of the twelve models in terms of R^2 and MSE.

Fig. 18 presents the parity plots of predicted vs. FEM-derived *FS* values for the twelve models. For KAN and MLP, most samples are distributed close to the $y = x$ reference line and remain largely within the ±15% error bounds. This distribution indicates good agreement between predicted and FEM-derived *FS* values.

CatBoost and LightGBM also show relatively compact point distributions, although their test samples exhibit slightly larger scatter than those of KAN and MLP. By contrast, DecisionTree and ExtraTree show more dispersed predictions, especially in the medium-to-high *FS* range. KNN and XGB fit the training samples very closely, but their test samples deviate more noticeably from the reference line, which is consistent with their larger train–test performance gaps.

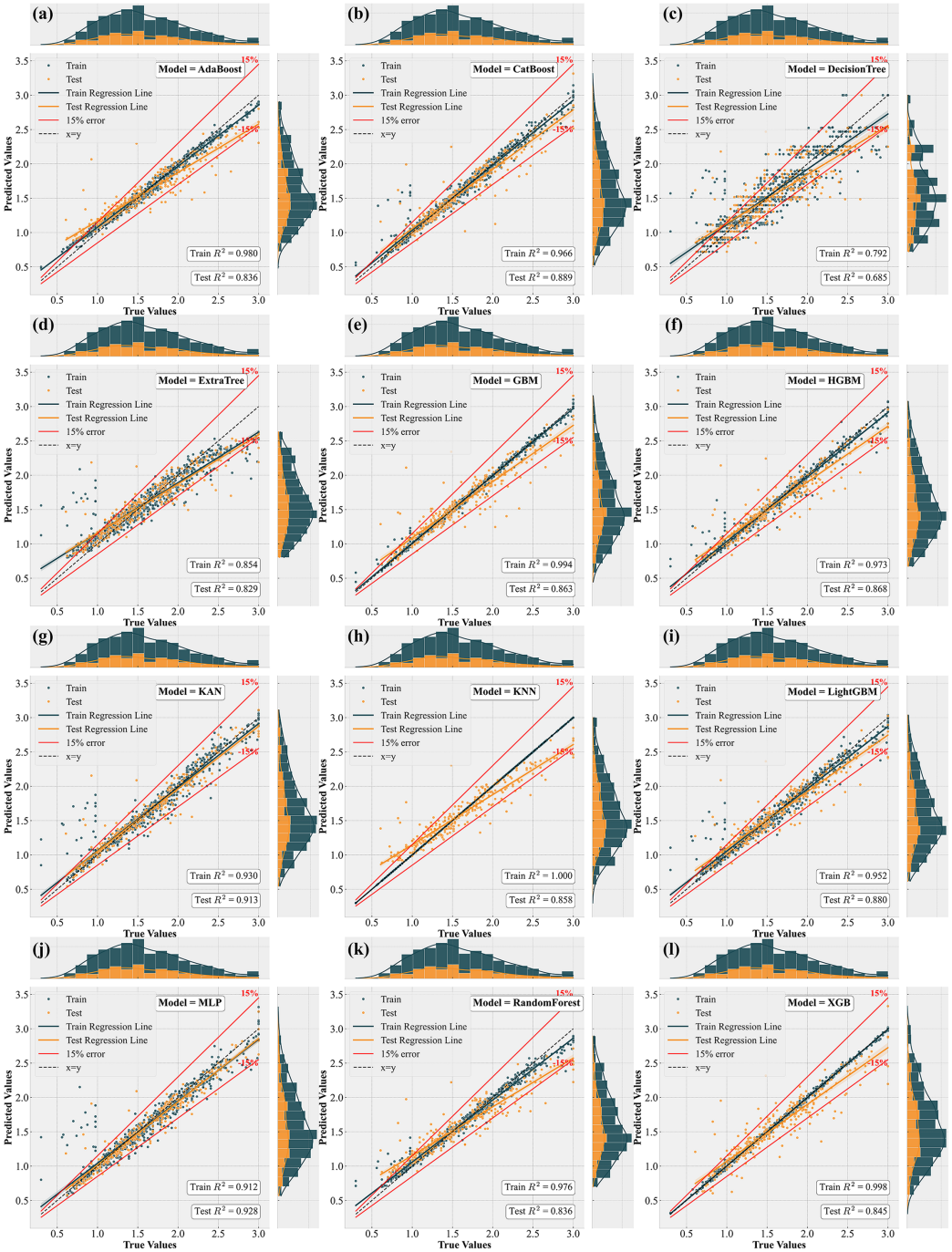


Figure 18: Parity plots of predicted vs. FEM-derived safety factors for the twelve machine learning models: (**a**) AdaBoost, (**b**) CatBoost, (**c**) DecisionTree, (**d**) ExtraTree, (**e**) GBM, (**f**) HGBM, (**g**) KAN, (**h**) KNN, (**i**) LightGBM, (**j**) MLP, (**k**) RandomForest, and (**l**) XGB.

Qi and Tang [18] compared six firefly-algorithm-optimized machine-learning classifiers using 148 field slope cases. Their results showed that SVM achieved the best test performance, with an AUC of 0.967 and an accuracy of 0.96, followed by GBM and Random Forest, whereas the multilayer perceptron neural network achieved an AUC of 0.864. In contrast, the present continuous *FS* regression identified MLP, KAN, and CatBoost as the leading group. This difference in model ranking is not contradictory because the two studies address different prediction tasks and data structures. Reference [18] classified ordinary slopes using field cases characterized by slope geometry, pore-water ratio, and soil properties, whereas the present study predicts continuous *FS* values from 1024 three-dimensional FEM cases of pile-reinforced slopes and explicitly includes pile position, diameter, and spacing ratio. Nevertheless, both studies indicate that nonlinear ensemble, kernel-based, or neural-network models generally outperform a single decision tree. These comparisons confirm that the optimal algorithm is dependent on the prediction objective, database source, and engineering variables rather than being universally superior.

Overall, MLP provided the strongest accuracy-oriented result on the selected test split, whereas KAN provided competitive accuracy together with an R^2 train–test gap of 0.017 and a model structure suitable for the subsequent SHAP analysis. KAN is therefore used as the primary model for interpretation and system demonstration, not claimed to be statistically more accurate than MLP. MLP is retained as the principal accuracy benchmark.

4.4 Paired Statistical Comparison of Model Performance

To determine whether the observed performance differences were statistically meaningful, paired statistical tests were conducted using the sample-wise absolute errors of the twelve models on the same 308 independent test samples. The overall differences were first assessed using the Friedman test. Pairwise Wilcoxon signed-rank tests with Holm correction were subsequently performed. In addition, paired bootstrap resampling with 10,000 repetitions was used to estimate the 95% confidence intervals of the RMSE and MAE differences between MLP and KAN.

Fig. 19 compares the distributions of the sample-wise absolute prediction errors. KAN, CatBoost, and MLP exhibited the most favorable overall error distributions, with mean absolute-error ranks of 4.672, 4.698, and 4.938, respectively. MLP achieved the lowest RMSE of 0.138, indicating better control of relatively large prediction errors. In contrast, KAN produced a slightly lower MAE and median absolute error than MLP, with corresponding values of 0.084 and 0.042. Thus, neither model was consistently superior across all error measures.

The Friedman test indicated a significant overall difference among the twelve models ($\chi^2(11) = 458.10$, $p < 0.001$), confirming that the model performances were not equivalent on the selected test set. The Holm-corrected pairwise results are summarized in Fig. 20. Significant differences were observed between the leading models and several lower-performing models. However, no statistically significant pairwise differences were detected among KAN, MLP, and CatBoost. For KAN and MLP, the Wilcoxon signed-rank test yielded a raw p-value of 0.325 and a Holm-adjusted p-value of 1.000. The rank-biserial effect size was −0.065, indicating only a small difference. KAN produced a lower absolute error for 53.6% of the test samples, whereas MLP performed better for 46.4%. These results show that the numerical differences between KAN and MLP were not statistically significant in terms of sample-wise absolute error.

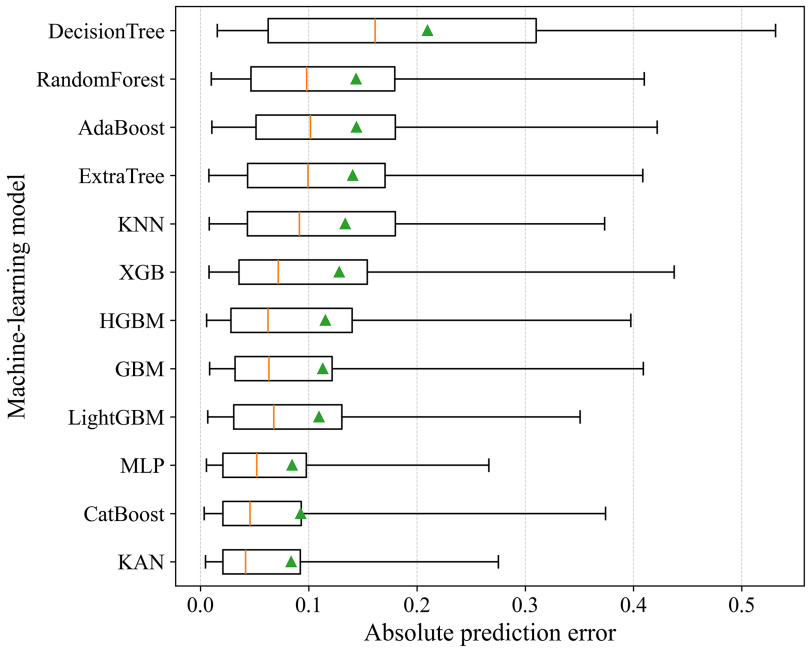


Figure 19: Distributions of sample-wise absolute prediction errors for the twelve machine-learning models on the independent test set.

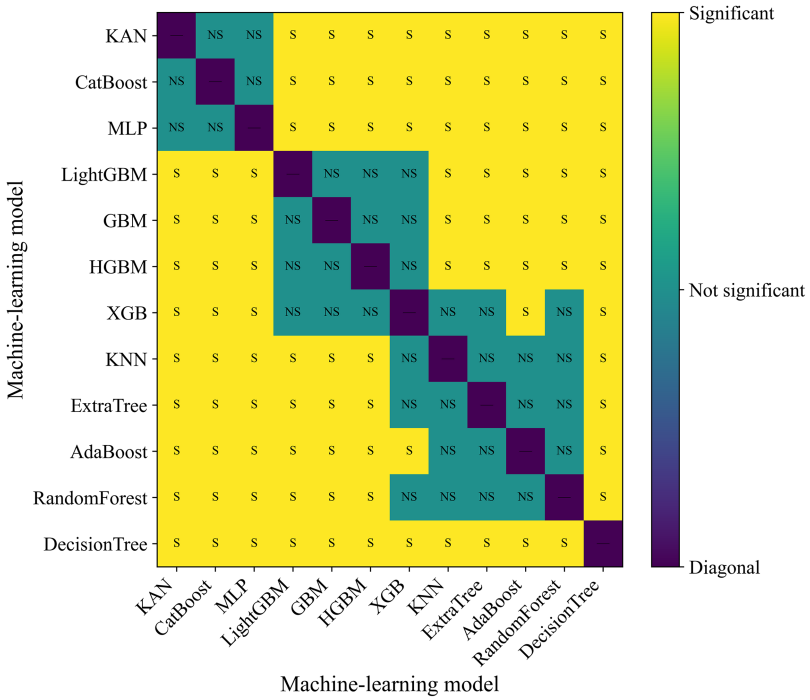


Figure 20: Pairwise statistical significance matrix of the twelve machine-learning models based on Wilcoxon signed-rank tests with Holm correction. S and NS denote statistically significant and nonsignificant differences at the 0.05 level, respectively.

The empirical cumulative distributions in Fig. 21 further show substantial overlap among KAN, MLP, and CatBoost, supporting their comparable error distributions. Although MLP achieved a lower RMSE than KAN, the paired bootstrap estimate of the RMSE difference, defined as $RMSE_{MLP} - RMSE_{KAN}$, was −0.0137, with a 95% confidence interval of [−0.0265, 0.0004]. The corresponding MAE difference was 0.0008, with a 95% confidence interval of [−0.0065, 0.0081]. Both intervals included zero.

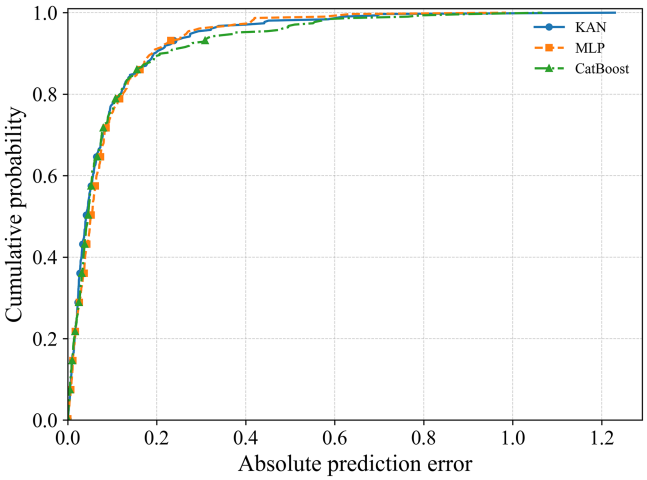


Figure 21: Empirical cumulative distributions of absolute prediction errors for KAN, MLP, and CatBoost.

Overall, MLP achieved the best accuracy-oriented performance, whereas KAN showed statistically comparable sample-wise errors, a slightly lower MAE and median absolute error, and a small train–test gap. KAN was therefore selected as the representative model for the subsequent database-size, additional-case, and SHAP analyses, while MLP was retained as the principal accuracy benchmark. This selection reflects the analytical focus of the present study rather than statistical superiority of KAN over MLP. These statistical conclusions are conditional on the selected independent test split and do not quantify the variability associated with alternative train–test partitions.

4.5 Database-Size Sensitivity Analysis of the Representative KAN Model

Based on the comparative and statistical results in Sections 4.3 and 4.4, KAN was selected as the representative model for evaluating database-size sensitivity. This choice was based on its competitive predictive performance and its role in the subsequent interpretation and system analyses, rather than on an assumption of statistical superiority over MLP. Nested Sobol subsets containing 128, 256, 512, 768, and 1024 samples were evaluated using three repetitions of five-fold cross-validation. The KAN architecture and training hyperparameters were kept unchanged for all subsets, and the mean and standard deviation of R^2, RMSE, and MAE were used to characterize prediction accuracy and variability. The resulting learning curves are shown in Fig. 22.

As shown in Fig. 22, increasing the database size consistently improved the mean prediction accuracy and generally reduced the variability among different data partitions. When the number of samples increased from 128 to 1024, the mean R^2 increased from 0.649 ± 0.188 to 0.895 ± 0.034. Over the same range, the mean RMSE decreased from 0.297 ± 0.069 to 0.170 ± 0.026, while the mean MAE decreased from 0.180 ± 0.037 to 0.085 ± 0.008. The substantial reduction in the standard deviations also indicates that model performance became less sensitive to the particular training–validation partition as the database expanded. The largest improvements occurred when the database size increased from 128 to 512 samples. Beyond 512 samples, the

learning curves gradually flattened. Increasing the database from 768 to 1024 samples improved the mean R^2 by only 0.0148, while the mean RMSE and MAE decreased by 4.75% and 5.62%, respectively. Meanwhile, the standard deviation of R^2 decreased from 0.063 to 0.034. These results indicate that the learning curve was approaching a plateau and that the 1024-sample database provides reasonably stable KAN performance within the investigated parameter domain.

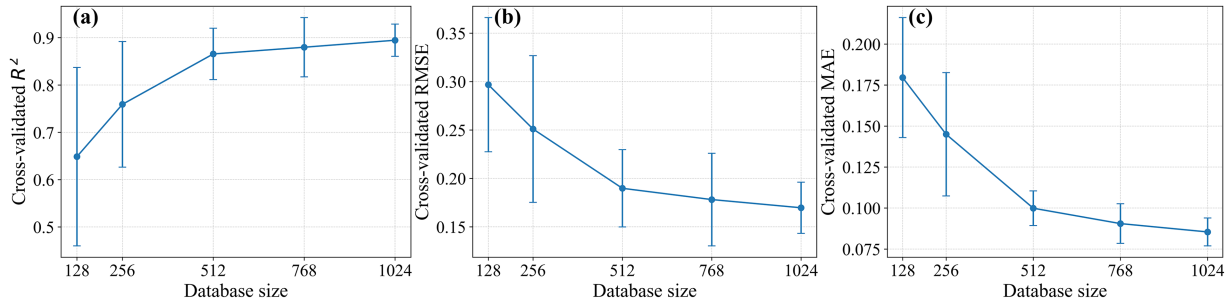


Figure 22: Database-size sensitivity of the KAN model based on three repetitions of five-fold cross-validation: (**a**) R^2; (**b**) RMSE; and (**c**) MAE.

4.6 Generalization Analysis of the Representative KAN Model

To further assess the predictive behavior of the representative KAN model, three additional cases were evaluated. These cases were not included in the training or test sets, but all input variables remained within the ranges listed in Table 4. The corresponding FEM-derived *FS* values and KAN-predicted *FS* values are shown in Fig. 23.

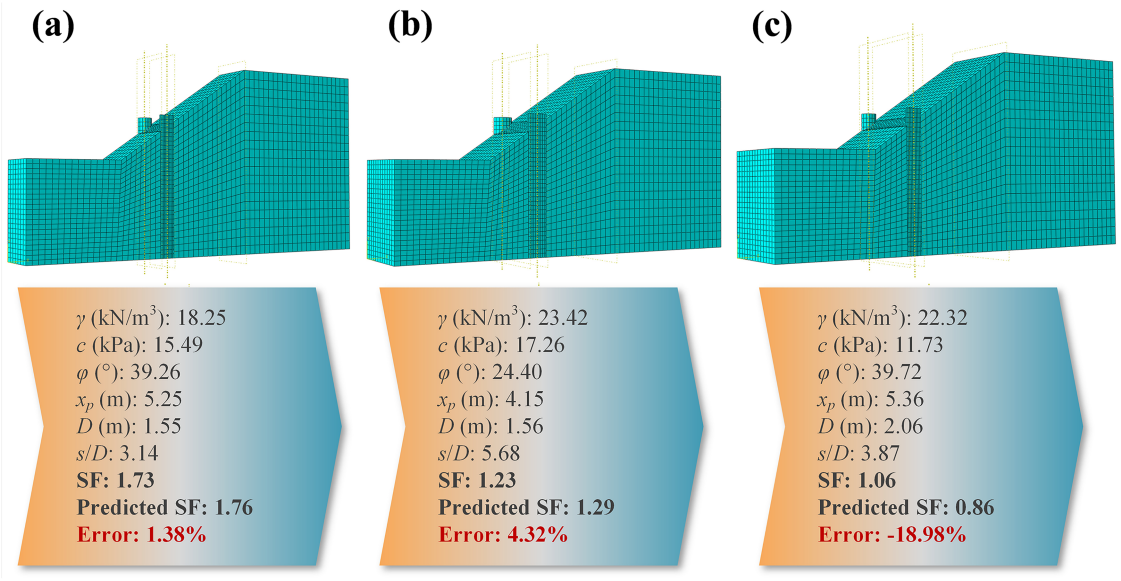


Figure 23: Representative generalization cases of the KAN model for pile-reinforced slope FS prediction: (**a**) Low-error, (**b**) Moderate-error, and (**c**) high-error cases.

As shown in Fig. 23a, KAN predicted the low-error case with an FEM-derived *FS* of 1.73, a predicted *FS* of 1.76, and a relative error of 1.38%. For the moderate-error case in Fig. 23b, the corresponding values were 1.23 and 1.29, with a relative error of 4.32%. In the high-error case (Fig. 23c), however, the FEM-derived *FS*

was 1.06 and the predicted *FS* was 0.86, giving a relative error of −18.98%. The results indicate that remaining within the prescribed input ranges does not guarantee uniformly low prediction errors for every parameter combination. FEM verification is therefore required for unusual parameter combinations, cases close to the stability threshold, and safety-critical or final-design applications.

5 SHAP-Based Interpretation and Software Implementation

Although the comparative results in Section 4.3 demonstrate the predictive capability of the developed machine-learning models, their practical use in slope engineering also requires interpretability and deployability. Engineers need to understand how different soil and pile parameters contribute to the predicted FS, rather than relying only on black-box numerical outputs. Therefore, SHAP analysis was introduced to quantify both the global and local contributions of input variables to *FS* prediction. Based on the comparative and statistical analyses, KAN was retained as the representative model for detailed SHAP interpretation, while MLP was used as the accuracy-oriented reference model. SHAP is model agnostic; therefore, the present analysis does not assume that KAN is intrinsically more interpretable than MLP. Instead, the two models were compared to determine whether their learned relationships were physically consistent and robust to model architecture. Furthermore, a machine-learning-based prediction system was developed to integrate parameter input, model inference, result visualization, and interpretability analysis, thereby supporting rapid stability assessment of pile-reinforced slopes.

5.1 Global SHAP Interpretation

To investigate the global feature importance of the developed machine-learning models, SHAP summary plots were generated for all twelve models, as shown in Fig. 24.

A consistent pattern was observed across most models. From a geotechnical perspective, cohesion c and friction angle φ dominate the prediction because they directly determine the mobilized Mohr–Coulomb shear resistance throughout the potentially deforming soil mass. Their influence is therefore more system-wide than that of the pile-layout variables, which mainly modify the local pile–soil interaction and load-transfer mechanisms. The negative contribution of unit weight γ reflects the increase in gravitational driving force. Pile diameter D affects pile stiffness and the transfer of soil reaction to the piles, whereas the spacing ratio s/D controls the overlap of adjacent pile restraint zones and the development of inter-pile soil arching. The latter interpretation is consistent with the physical tests, in which the smaller spacing ratio produced more pronounced arch-shaped cracking, stronger earth-pressure concentration between the piles, and larger pile bending responses. The comparatively small contribution of pile position x_p should be interpreted within the fixed slope geometry and sampled parameter interval adopted in this study.

Among the twelve models, the representative KAN model exhibited a physically consistent SHAP pattern. In Fig. 24g, c and φ remain the two dominant variables, followed by D, while s/D and γ play secondary roles and x_p has only a minor global influence. The ordering of feature importance identified by KAN is broadly consistent with the established understanding that soil strength parameters primarily govern slope stability, whereas pile geometric parameters provide supplementary control. This agreement between SHAP-based interpretation and engineering intuition further supports the physical consistency of the KAN-based interpretation.

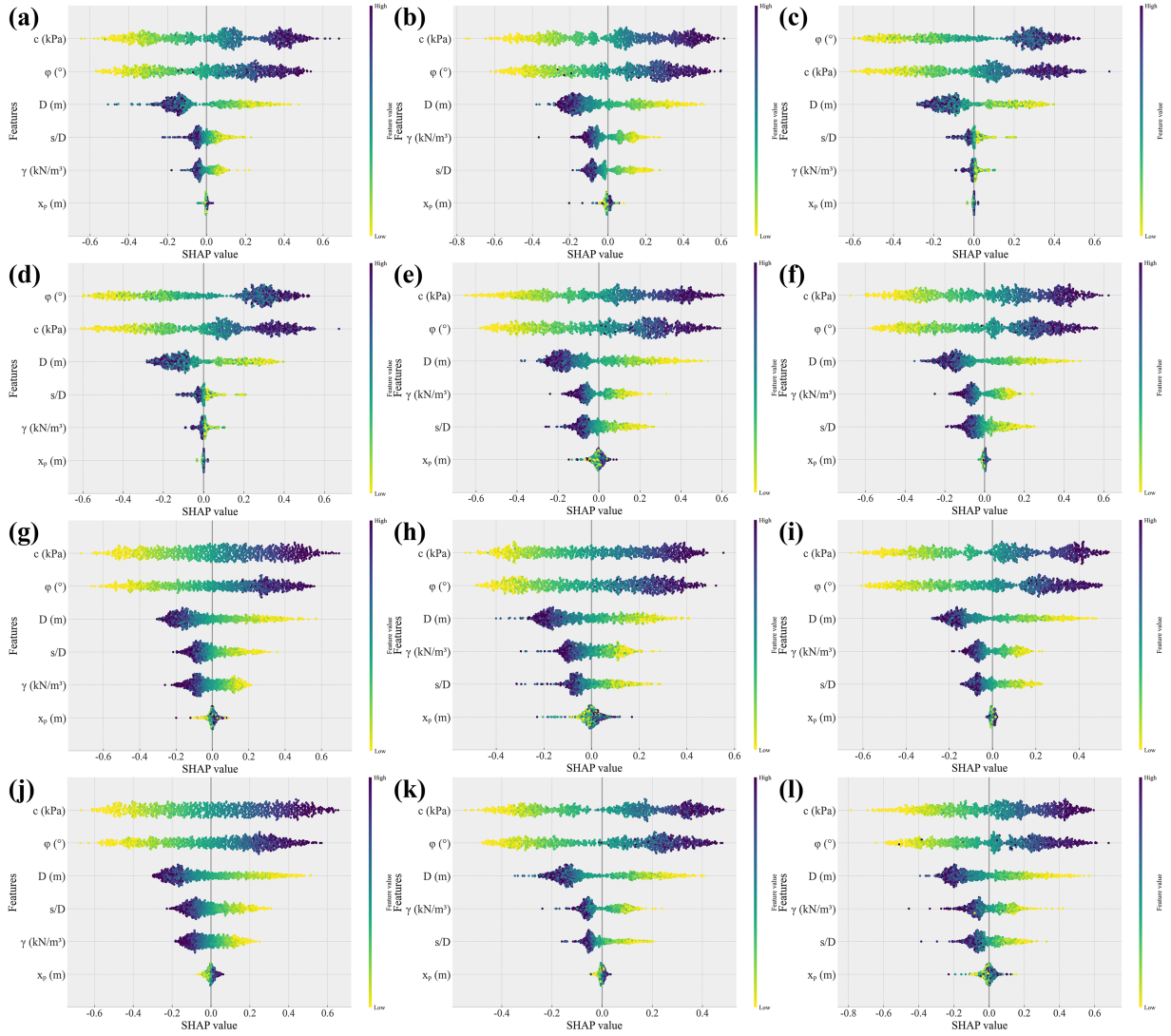


Figure 24: SHAP summary plots for safety factor prediction using the twelve machine learning models: (**a**) AdaBoost, (**b**) CatBoost, (**c**) DecisionTree, (**d**) ExtraTree, (**e**) GBM, (**f**) HGBM, (**g**) KAN, (**h**) KNN, (**i**) LightGBM, (**j**) MLP, (**k**) RandomForest, and (**l**) XGB.

5.2 Quantitative Feature Contribution and Local SHAP Explanation

Normalized mean absolute SHAP values quantified the relative feature contributions of the twelve models, as shown in Fig. 25. The results are generally consistent with the SHAP summary plots in Fig. 24. Soil cohesion c and friction angle φ contribute the most to FS prediction in most models, followed by pile diameter D. In contrast, spacing ratio s/D, soil unit weight γ, and pile position x_p show relatively smaller contributions. Across the twelve models, the combined contribution of c and φ is generally close to or greater than 60%, indicating that soil strength parameters dominate the predicted stability response of pile-reinforced slopes. Qi and Tang [18] also identified cohesion as the most influential variable, with an importance score of 0.310, followed by friction angle and unit weight. This ranking is broadly consistent with the present SHAP results, although their analysis concerned unreinforced-slope classification rather than FS regression for pile-reinforced slopes.

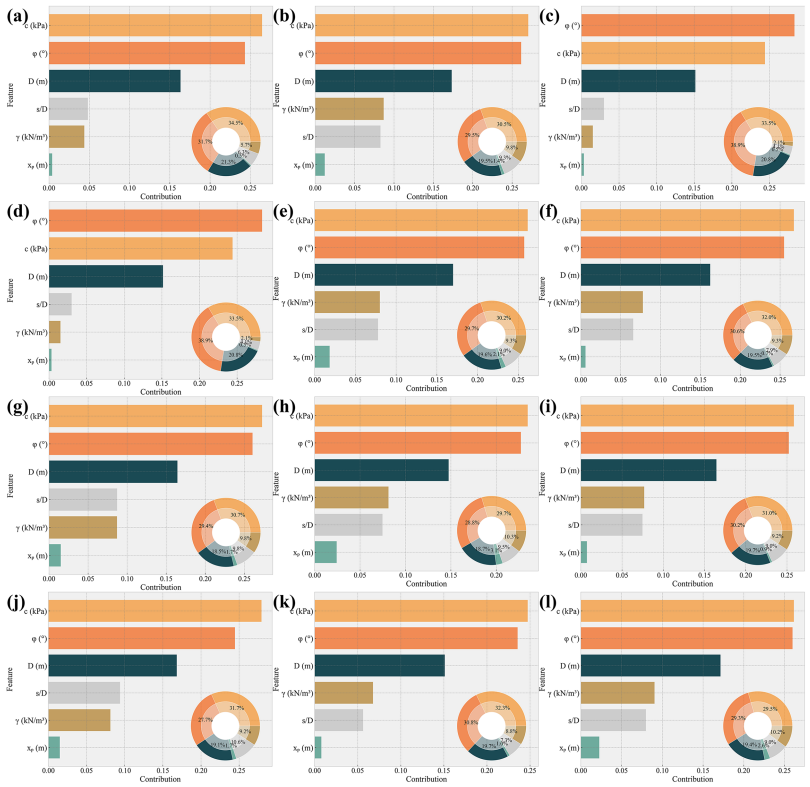


Figure 25: SHAP-based feature contribution analysis for safety factor prediction using the twelve machine learning models: (**a**) AdaBoost, (**b**) CatBoost, (**c**) DecisionTree, (**d**) ExtraTree, (**e**) GBM, (**f**) HGBM, (**g**) KAN, (**h**) KNN, (**i**) LightGBM, (**j**) MLP, (**k**) RandomForest, and (**l**) XGB.

The effectiveness of these geometric mechanisms also depends on soil strength. Higher cohesion and friction angle enable the inter-pile soil to sustain a stronger stress arch and transfer more sliding thrust to the piles, whereas weaker soil conditions may limit the mobilization of soil arching. Therefore, the effects of D and s/D should be interpreted as coupled pile–soil responses rather than independent one-dimensional relationships.

For the representative KAN model, the contribution pattern is physically reasonable and consistent with engineering expectations. As shown in Fig. 25g, cohesion and friction angle contributed 30.7% and 29.4%, respectively, jointly accounting for 60.1% of the normalized mean absolute SHAP contribution. Pile diameter ranked third with a contribution of 18.5%, followed by spacing ratio and unit weight, both approximately 9.8%, while pile position contributed only 1.7%. This feature hierarchy is consistent with the principal geotechnical mechanisms represented in the FEM database.

The feature-dependence relationships of KAN and MLP are shown in Figs. A1 and A2. Increasing c and φ generally produces positive SHAP values because it increases mobilized shear resistance, whereas increasing γ produces negative contributions by increasing the gravitational driving force. The effect of D is model dependent because a larger diameter changes both pile stiffness and the absolute spacing s implied by a given s/D. Increasing s/D generally reduces the SHAP contribution, consistent with the physical tests: wider spacing weakens cooperative pile restraint and the transfer of sliding thrust through an inter-pile soil arch. These coupled trends explain why geometric variables have lower global importance than c and φ but remain relevant under specific parameter combinations. The agreement between KAN and MLP for the principal soil parameters indicates that these physically meaningful relationships are not specific to a single model architecture.

To examine the prediction mechanism at the individual-sample level, local SHAP explanations of KAN and MLP were compared, as shown in Fig. 26. For the selected sample, the predicted *FS* values of KAN and MLP are 1.55 and 1.47, respectively. In both models, cohesion c and friction angle φ provide positive contributions to the predicted *FS*. In contrast, a larger spacing ratio s/D, unit weight γ, and pile diameter D reduce predictions relative to the baseline. The local explanation therefore agrees with the global SHAP results, confirming that the soil strength parameters are the main stabilizing factors, while pile layout and self-weight-related parameters may reduce or modify the stability response depending on their values.



Figure 26: Local SHAP explanation of FS prediction for the selected sample: (**a**) KAN and (**b**) MLP.

5.3 Development of a Machine-Learning-Based FS Prediction System

To improve practical usability, an interactive research prototype was established for pile-reinforced slopes. The system integrates trained models, parameter management, single-case and batch prediction, model comparison, and SHAP-based interpretation. Once a model is loaded, inference avoids repeated finite element strength-reduction runs and is therefore suitable for rapid preliminary screening and sensitivity exploration. It is not a substitute for project-specific design verification.

Fig. 27 shows the single-case prediction interface of the developed system. Users can input six key parameters, including soil unit weight γ, cohesion c, friction angle φ, pile position x_p, pile diameter D, and spacing ratio s/D. After the input parameters are specified, the system automatically calls the integrated trained models and outputs the predicted *FS* values. The prediction results of different models are displayed simultaneously, allowing users to compare the responses of multiple algorithms under the same engineering condition. This design improves the transparency of model selection and provides a convenient basis for preliminary stability assessment.

The visualization and interpretation module is shown in Fig. 28. It provides model-performance comparison, local SHAP explanation, and feature-importance ranking. The system is restricted to the six inputs and the slope and pile configuration represented by the database. It does not explicitly account for layered or spatially variable ground, groundwater variation, alternative pile layouts, seismic loading, or construction effects. Users should therefore check that all inputs fall within Table 4 and perform finite element verification for out-of-domain, safety-critical, or final-design applications.

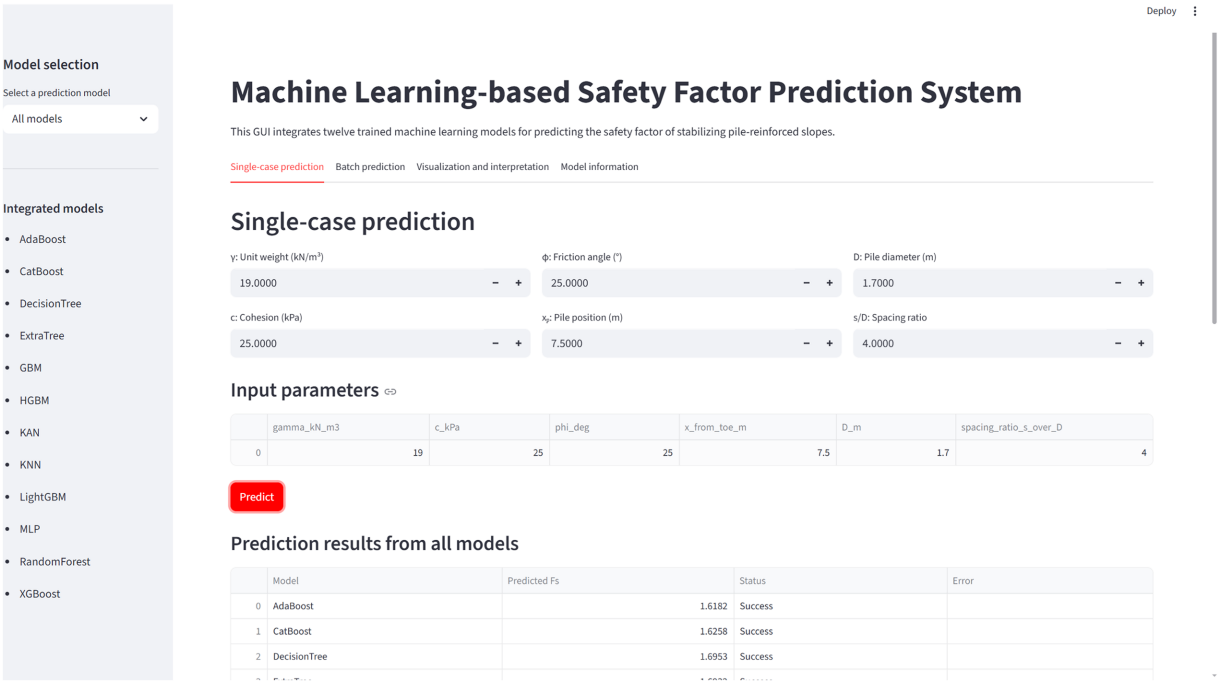


Figure 27: Prediction interface of the machine-learning-based safety factor prediction system.

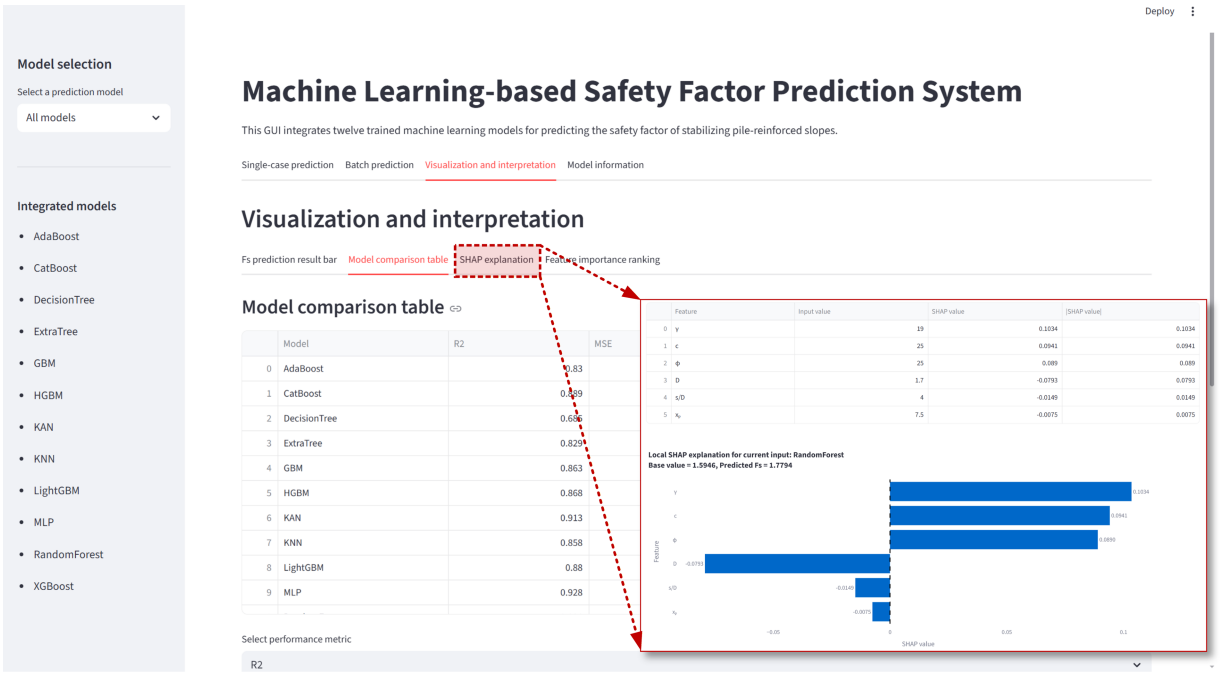


Figure 28: Visualization and interpretation module of the machine-learning-based safety factor prediction system.

The platform is intended for preliminary screening, rapid comparison of parameter combinations, batch prediction, and SHAP-based interpretation. Since it directly calls pre-trained models, routine prediction can be performed on a conventional desktop or laptop computer without a dedicated GPU. Its application should remain within the parameter ranges and slope configuration represented by the present database.

5.4 Applicability and Future Extension

The proposed framework is developed for rapid *FS* prediction of pile-reinforced slopes within the parameter space and structural configuration represented by the present FEM database. The current model considers six principal variables describing soil strength, unit weight, pile position, pile diameter, and spacing ratio. Within this domain, the framework provides an efficient tool for preliminary stability assessment, model comparison, and parameter-sensitivity analysis.

Application to substantially different geological conditions, reinforcement layouts, or loading scenarios requires corresponding extension of the training database. For example, layered ground, groundwater variation, alternative pile arrangements, or additional environmental and dynamic loads may introduce response mechanisms that are not fully represented by the current input set. In such cases, the present workflow can be extended by introducing additional variables, generating new FEM samples, and retraining the surrogate models.

Therefore, the trained models should primarily be used for cases that are consistent with the ranges and configuration summarized in Table 4. For conditions beyond this domain, supplementary numerical verification or database enrichment is recommended. The modular structure of the proposed framework allows these extensions to be incorporated without changing the overall experimental–numerical–data-driven methodology.

6 Conclusion

This study developed an experimental–numerical–data-driven framework for rapid and interpretable FS prediction of pile-reinforced slopes. The main scientific contribution lies in linking physical observations of pile–soil interaction with three-dimensional FEM database construction, statistical comparison of multiple surrogate models, and SHAP-based engineering interpretation. The principal conclusions are as follows.

1. The physical tests demonstrated that pile spacing significantly affects inter-pile soil arching, earth-pressure redistribution, and pile bending response. The smaller spacing ratio produced more pronounced arch-shaped cracking and stronger load transfer to the piles, providing a physical basis for interpreting the influence of pile-layout variables.
2. The three-dimensional FEM model incorporating cohesion anisotropy reproduced the principal deformation pattern, soil-arching evolution, and dominant pile-bending region observed in the tests. This agreement indicates that the model reasonably represents the principal pile–soil interaction response under this condition.
3. A Sobol-sampled database containing 1024 FEM cases was constructed using six soil and pile-layout variables. The centered-discrepancy analysis confirmed progressively improved coverage of the input space, while the KAN learning curves showed increasingly stable prediction performance as the database size increased.
4. Among the twelve models, MLP achieved the highest test-set accuracy, whereas KAN exhibited statistically comparable sample-wise errors and a slightly lower MAE and median absolute error. KAN was therefore selected as the representative model for database-size, additional-case, and SHAP analyses, while MLP was retained as the accuracy-oriented benchmark. This selection reflects the analytical focus of the study rather than statistical superiority of KAN.
5. The SHAP results showed that cohesion and friction angle dominate FS prediction because they directly control the mobilized shear resistance. Pile diameter and spacing ratio influence stability through pile stiffness, pile–soil load transfer, and soil arching. The developed platform can support rapid preliminary

screening, comparison of parameter combinations, and sensitivity interpretation without repeated FEM strength-reduction analyses.

The present framework is established for the parameter ranges and pile-reinforced slope configuration represented in the current database. Its extension to more complex geological conditions, alternative reinforcement layouts, and additional loading scenarios requires corresponding expansion of the FEM database and input variables. Future work will focus on these extensions together with broader experimental and engineering validation.

Acknowledgement: None.

Funding Statement: Financial support from the Fundamental Research Funds for the Central Universities (No. 2242022k30062), and the National Natural Science Foundation of China (No. 52278155) is gratefully acknowledged.

Author Contributions: The authors confirm their contributions to the paper as follows: study conception and design: Jingqiu Yang, Wei Li, and Jun Jiang; data collection: Huan Zheng, Jinlong Pan, and Li Guo; data analysis and interpretation of results: Jingqiu Yang, Wei Li, Huan Zheng, and Jinlong Pan; draft manuscript preparation: Jingqiu Yang and Wei Li; manuscript review and revision: Huan Zheng, Jinlong Pan, Jun Jiang, and Li Guo; supervision and project administration: Li Guo. All authors reviewed and approved the final version of the manuscript.

Availability of Data and Materials: Data will be made available upon request with the consent of the corresponding author.

Ethics Approval: Not applicable.

Conflicts of Interest: The authors declare no conflicts of interest.

Appendix A

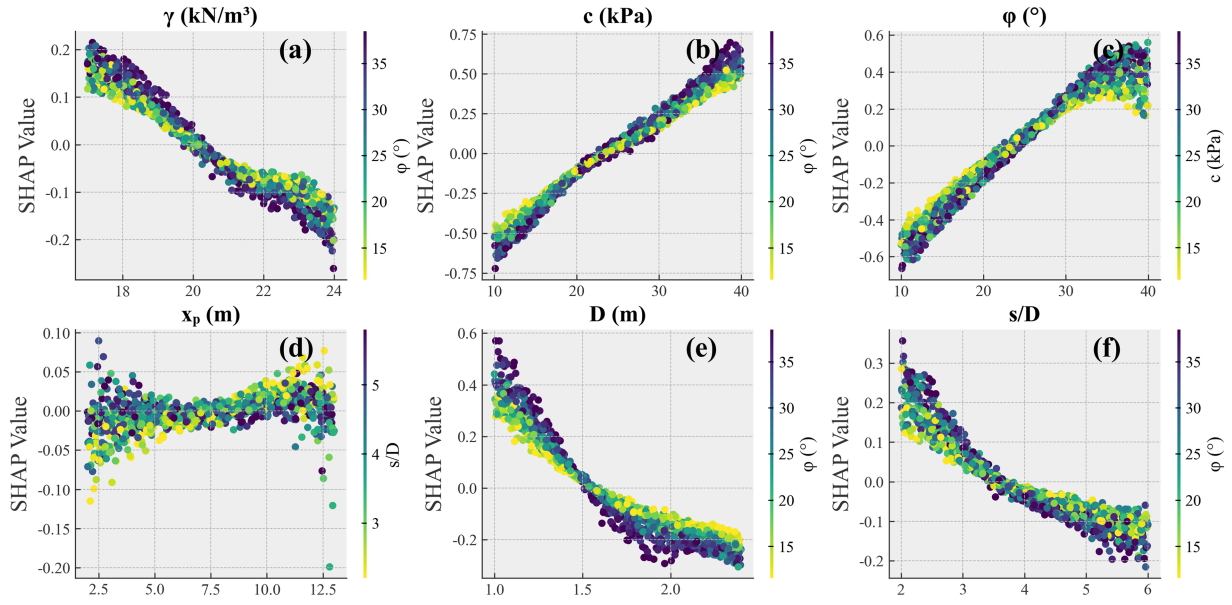


Figure A1: SHAP dependence plots of key input variables for FS prediction using the KAN model: (**a**) Unit weight γ; (**b**) Cohesion c; (**c**) Friction angle φ; (**d**) Pile position x_p; (**e**) Pile diameter D; and (**f**) Spacing ratio s/D.

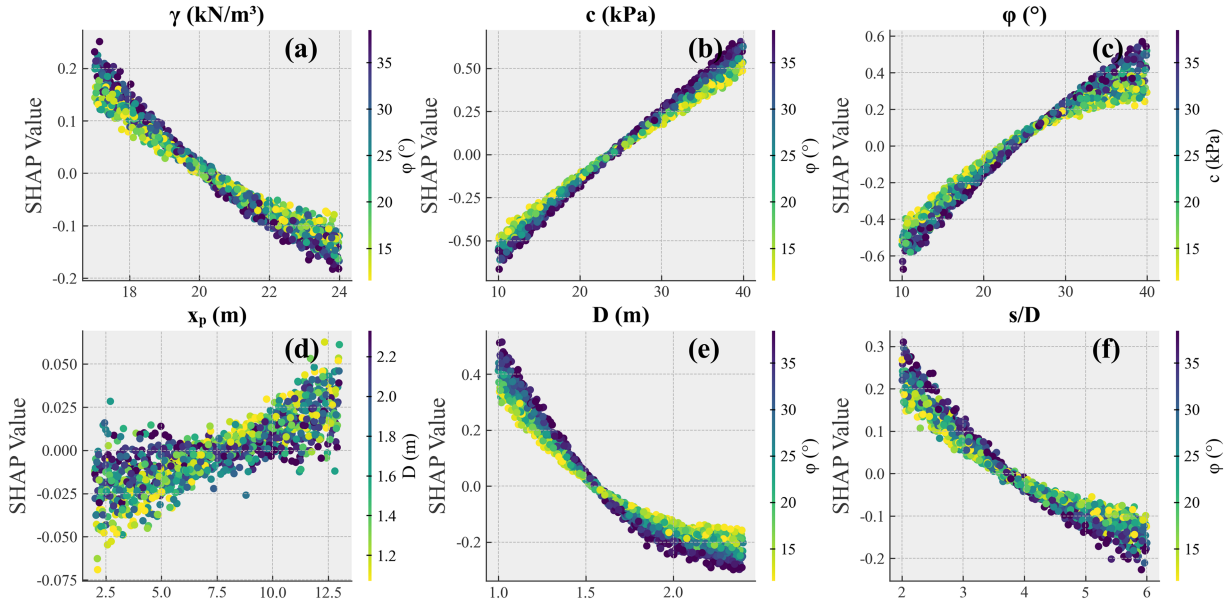


Figure A2: SHAP dependence plots of key input variables for FS prediction using the MLP model: (**a**) Unit weight γ; (**b**) Cohesion c; (**c**) Friction angle φ; (**d**) Pile position x_p; (**e**) Pile diameter D; and (**f**) Spacing ratio s/D.

References

1. Kourkoulis R, Gelagoti F, Anastasopoulos I, Gazetas G. Hybrid method for analysis and design of slope stabilizing piles. J Geotech Geoenviron Eng. 2012;138(1):1–14. doi:10.1061/(asce)gt.1943-5606.0000546.
2. Chen Q, Xu C, Zou B, Luo Z, Xu C, Long X. Earth pressure of the trapdoor problem using three-dimensional discrete element method. Comput Model Eng Sci. 2023;135(2):1503–20. doi:10.32604/cmes.2022.022823.
3. Zhang S, Li C, Qi H, Chen X, Ma S. Soil arch evolution characteristics and parametric analysis of slope anchored anti-slide pile. KSCE J Civ Eng. 2021;25(11):4121–32. doi:10.1007/s12205-021-1612-6.
4. Shangguan Y, Xue D, Wang G, Li D, Bao S, Wang W. A study on soil arching effect of anti-slide pile considering different pile arrangements. Front Earth Sci. 2023;11:1195552. doi:10.3389/feart.2023.1195552.
5. Dawson EM, Roth WH, Drescher A. Slope stability analysis by strength reduction. Géotechnique. 1999;49(6):835–40. doi:10.1680/geot.1999.49.6.835.
6. Griffiths DV, Lane PA. Slope stability analysis by finite elements. Géotechnique. 1999;49(3):387–403. doi:10.1680/geot.1999.49.3.387.
7. Xu H, He X, Pradhan B, Sheng D. A pre-trained deep-learning surrogate model for slope stability analysis with spatial variability. Soils Found. 2023;63(3):101321. doi:10.1016/j.sandf.2023.101321.
8. Wang L, Jia H, Jiang T, Zhang J, Jia Y, Li L, et al. Novel evaluation method based on critical arch height as instability criterion for sustaining arch locked-segment-type slopes. Sci Rep. 2024;14(1):7991. doi:10.1038/s41598-024-58737-w.
9. He Y, Li Z, Wang W, Yuan R, Zhao X, Nikitas N. Slope stability analysis considering the strength anisotropy of c-φ soil. Sci Rep. 2022;12(1):18372. doi:10.1038/s41598-022-20819-y.
10. Aminpour M, Alaie R, Khosravi S, Kardani N, Moridpour S, Nazem M. Slope stability machine learning predictions on spatially variable random fields with and without factor of safety calculations. Comput Geotech. 2023;153(4):105094. doi:10.1016/j.compgeo.2022.105094.
11. Mahmoodzadeh A, Mohammadi M, Farid Hama Ali H, Hashim Ibrahim H, Nariman Abdulhamid S, Nejati HR. Prediction of safety factors for slope stability: comparison of machine learning techniques. Nat Hazards. 2022;111(2):1771–99. doi:10.1007/s11069-021-05115-8.
12. Khajehzadeh M, Keawsawasvong S. Predicting slope safety using an optimized machine learning model. Heliyon. 2023;9(12):e23012.

13. Li Y, Sun Z, Li Y, Yang H, Liu X, He W. A vision transformer-based method for predicting seismic damage states of RC piers: database development and efficient assessment. Reliab Eng Syst Saf. 2025;263(2):111287. doi:10.1016/j.ress.2025.111287.
14. Li Y, Sun Z, Mangalathu S, Li Y, He W, Xue X. Machine learning-based full-life-cycle seismic response assessment for in-service bridge piers: comprehensive analysis of interpretability and seismic fragility. Structures. 2025;80:110050. doi:10.1016/j.istruc.2025.110050.
15. Sun Z, Li Y, Yang Y, Su L, Xie S. Splitting tensile strength of basalt fiber reinforced coral aggregate concrete: optimized XGBoost models and experimental validation. Constr Build Mater. 2024;416(8):135133. doi:10.1016/j.conbuildmat.2024.135133.
16. Sun Z, Li Y, Su L, Liu S, Chen Z. Predicting corrosion behaviour of steel reinforcement in eco-friendly coral aggregate concrete based on hybrid machine learning methods. Nondestruct Test Eval. 2025;40(4):1334–54. doi:10.1080/10589759.2024.2349243.
17. Kewalramani M, Ghodhbani R, Mahmoodzadeh A, Alghamdi A, Karim FK, Alanazi A, et al. Predicting the compressive strength of sustainable concrete containing recycled aluminum beverage cans crumb using machine learning techniques. Comput Model Eng Sci. 2026;147(3):1–10. doi:10.32604/cmes.2026.084696.
18. Qi C, Tang X. Slope stability prediction using integrated metaheuristic and machine learning approaches: a comparative study. Comput Ind Eng. 2018;118(1):112–22. doi:10.1016/j.cie.2018.02.028.
19. Zheng S, Jiang AN, Feng KS. A reliability evaluation method for intermittent jointed rock slope based on evolutionary support vector machine. Comput Model Eng Sci. 2021;129(1):149–66. doi:10.32604/cmes.2021.016761.
20. Ahmad F, Tang X, Hu J, Ahmad M, Gordan B. Improved prediction of slope stability under static and dynamic conditions using tree-based models. Comput Model Eng Sci. 2023;137(1):455–87. doi:10.32604/cmes.2023.025993.
21. Sun Z, Han T, Wang X, Wang L, Fu H, Li Y, et al. Bidirectional mapping modeling of pipeline vertical deformation and axial strain based on multi-source monitoring data and machine learning. J Pipeline Sci Eng. 2026;16(4):100432. doi:10.1016/j.jpse.2026.100432.
22. Liu J, Kong X, Wang S, Peng L, Wang Q, Zhang Y, et al. Multi-objective material-structure integrated optimization of recycled aggregate CFST stub columns for mechanical performance, reliability, and sustainability. Expert Syst Appl. 2026;324(4):132597. doi:10.1016/j.eswa.2026.132597.
23. Li Y, Sun Z, Mangalathu S, Li Y, Yang H, He W. Seismic damage states prediction of in-service bridges using feature-enhanced swin transformer without reliance on damage indicators. Eng Appl Artif Intell. 2025;159(2):111651. doi:10.1016/j.engappai.2025.111651.
24. Tun SH, Zeng C, Jamil F. Prediction of slope stability based on five machine learning techniques approaches: a comparative study. Multiscale Multidiscip Model Exp Des. 2025;8(5):224. doi:10.1007/s41939-025-00808-0.
25. Chen Y, Kong J, Lou Y, Zhang X, Li J, Ling D. Slope stability prediction using multi-stage machine learning with multi-source data integration strategy. Can Geotech J. 2025;62(177):1–18. doi:10.1139/cgj-2025-0069.
26. Huang N, Han Y, Xie W, Hu R, Peng H, Song G, et al. An innovative and efficient approach for slope reliability analysis: machine learning based surrogate modeling with advanced attention mechanisms. Eng Geol. 2025;354(4):108194. doi:10.1016/j.enggeo.2025.108194.
27. Li W, Ma G, Jiang M, Xu J, Rezania M, Zhu H. An efficient graph neural networks surrogate model for slope reliability analysis considering soil spatial variability. Reliab Eng Syst Saf. 2026;267:111924. doi:10.1016/j.ress.2025.111924.
28. Li Y, Guan J, Guo L. Peridynamic-driven feature-enhanced vision transformer for predicting defects and heterogeneous materials locations: applications of deep learning in inverse problems. Eng Appl Artif Intell. 2025;151(14):110677. doi:10.1016/j.engappai.2025.110677.
29. Lundberg M, Lee SI. A unified approach to interpreting model predictions. arXiv:1705.07874. 2017.
30. Lin H, Li L, Qiang Y, Zhang Y, Liang S, Xu X, et al. Sensitivity analysis of slope stability based on eXtreme gradient boosting and SHapley additive exPlanations: an exploratory study. Heliyon. 2024;10(16):e35871. doi:10.1016/j.heliyon.2024.e35871.
31. Liu Z, Wang Y, Vaidya S, Ruehle F, Halverson J, Soljačić M, et al. KAN: kolmogorov-Arnold networks. arXiv:2404.19756. 2024.

32. Jose D, Kolathayar S, Nayak S. 3D finite element analysis of anti-slide pile performance for slope stabilization. Geotech Geol Eng. 2025;43(2):74. doi:10.1007/s10706-024-03043-5.
33. Benmebarek MA, Benmebarek S, Rad MM, Ray R. Pile optimization in slope stabilization by 2D and 3D numerical analyses. Int J Geotech Eng. 2022;16(2):211–24. doi:10.1080/19386362.2021.1972628.
34. Chen CY, Chang CK, Lin YS. Numerical analysis of pile—slope stability and the soil arching around two adjacent piles. J Mt Sci. 2022;19(11):3270–85. doi:10.1007/s11629-021-7260-y.
35. Du P, Liu X, Zhou D, Feng C. Influence and bearing mechanisms of thorn shape on compressive characteristics of thorn piles. Buildings. 2025;15(18):3328. doi:10.3390/buildings15183328.
36. Liu Z, Duan L, Zhang Y, Shen L, Yuan P. Deformation response and load transfer mechanism of collar monopile foundations in saturated cohesive soils. Buildings. 2025;15(14):2392. doi:10.3390/buildings15142392.
37. Wei W, Tang H, Song X, Ye X. 3D slope stability analysis considering strength anisotropy by a micro-structure tensor enhanced elasto-plastic finite element method. J Rock Mech Geotech Eng. 2025;17(3):1664–84. doi:10.1016/j.jrmge.2024.03.038.
38. Wang D, Jin X. Slope stability analysis by finite elements considering strength anisotropy. Rock Soil Mech. 2008;(3):667–72. doi:10.16285/j.rsm.2008.03.045.
39. Zhang Y, Wang Z, Liu J, Li Y, Huang Z, Yu X. A metaheuristic-driven categorical boosting framework with interpretability for high-precision prediction of mechanical properties in corroded reinforced concrete beams. Eng Appl Artif Intell. 2026;163(3):112804. doi:10.1016/j.engappai.2025.112804.
40. Sun Z, Wang X, Han T, Liu J, Wang L, Wei X, et al. Advanced prediction of pipeline vertical deformation and axial strain via multi-source data fusion and multi-task deep learning. Struct Health Monit. 2025. doi:10.1177/14759217251385078.
41. Sun Z, Wang X, Han T, Wang L, Zhu Z, Huang H, et al. Pipeline deformation prediction based on multi-source monitoring information and novel data-driven model. Eng Struct. 2025;337(10):120461. doi:10.1016/j.engstruct.2025.120461.
42. Yu X, Li J, Liu J, Li Y, Chen A, Zhang Y, et al. Cross-scenario impact damage prediction in concrete using peridynamics-trained Kolmogorov–Arnold networks with transfer learning. Int J Impact Eng. 2026;215:105764. doi:10.1016/j.ijimpeng.2026.105764.
43. Wang K, Shen T, Liu J, Wang S, Bao X, Wei J, et al. Exploration of computational formulations for wind-induced interference effects on high-rise buildings via Kolmogorov–Arnold networks. Dev Built Environ. 2025;24:100770. doi:10.1016/j.dibe.2025.100770.
44. Sun Z, Li Y, Han T, Su L, Zhu X, He J, et al. Performance evaluation of hybrid fiber-reinforced concrete based on electrical resistivity: experimental and data-driven method. Constr Build Mater. 2024;446(3):137992. doi:10.1016/j.conbuildmat.2024.137992.
45. Liu J, Wang S, Chen K, Wang K, Fan Y, Wang Q. Synthetic data augmentation and Integrated prediction framework for low-carbon recycled concrete: leveraging CTGAN and multiple ML models stacking. J Clean Prod. 2026;543:147599. doi:10.1016/j.jclepro.2026.147599.
46. Kong X, Fan Y, Liu J, Xi M, Zhang Y, Yu Y. Lightweight Kolmogorov-Arnold network with dual-objective optimization for axial capacity prediction of square coal gangue concrete-filled steel tube stub columns based on finite element simulation. Eng Appl Artif Intell. 2026;176:114843. doi:10.1016/j.engappai.2026.114843.
47. He X, Liu J, Li J, Yang Z, Kong X, Zhang Y, et al. Toward intelligent pavement maintenance: a transferable deep learning framework for cross-domain crack segmentation and UAV-based field inspection. Adv Eng Inform. 2026;73:104582. doi:10.1016/j.aei.2026.104582.
48. Li Y, Guan J, Guo L. Peridynamics-driven two-stage conditional diffusion generative model for discontinuous fracture prediction in porous structure. Adv Eng Inform. 2026;69:104090. doi:10.1016/j.aei.2025.104090.